EarthArXiv Coversheet

Authors

Andrew Gunn[1,♣] & Douglas J. Jerolmack[1,2,♠]

Affiliations

[1]Department of Earth and Environmental Sciences, University of Pennsylvania, Philadelphia, USA
[2]Department of Mechanical Engineering and Applied Mechanics, University of Pennsylvania, Philadelphia, USA

Emails

[♣]andle@sas.upenn.edu
[♠]sediment@sas.upenn.edu

Conditions for aeolian transport in the Solar System

Andrew Gunn[1] and Douglas J. Jerolmack[1,2,*]

[1]Department of Earth and Environmental Sciences, University of Pennsylvania, Philadelphia, USA
[2]Department of Mechanical Engineering and Applied Mechanics, University of Pennsylvania, Philadelphia, USA
[*]e-mail: sediment@sas.upenn.edu

ABSTRACT

Sand dunes arise wherever loose sediment is mobilized by winds that exceed threshold speeds, and grains are sufficiently strong to survive collisions[1]. The ubiquity of dunes in our solar system is remarkable and confounding[2]; their occurrence under conditions of thin atmospheres[3], and/or friable materials[4], challenges our understanding of sediment transport mechanics. Current threshold theories lose meaning and diverge from one another when extrapolated to some planetary bodies[5–9], because they neglect physical processes that become relevant under such exotic conditions. Here we draw on results in contact[10], rarified gas[11], statistical[12] and adhesion[13] mechanics to present more complete theories for the 'fluid' and 'impact' thresholds of aeolian transport. Our theoretical predictions compare well with all available experimental threshold observations, and shed light on the contentious issues of sediment mineralogy on Titan[4] and the high threshold for dune activity on Mars[14]. This work will aid in interpreting planetary atmospheric dynamics from observed dunes, and determining what observations are required for future space missions.

Sand dunes form when a ready supply of loose and durable grains is regularly entrained by wind into saltation, but rarely suspended[1,15]. On Earth, the presence of sand dunes is inextricably linked to climate; arid regions with large diurnal temperature swings limit cohesion and adhesion forces that resist grain motion, while promoting strong surface winds capable of transporting sand[16]. The relevant fluid and particle forces are encapsulated in the threshold friction velocity u_*, which describes the required surface wind conditions for particle entrainment and hence dune formation. Theoretical derivations of threshold u_*, calibrated in wind tunnels and vetted in field observations[5–9], provide satisfactory explanations for dune-forming conditions on Earth. Ever expanding observations across our Solar System, however, have revealed surprises; in particular, dunes seem to be more ubiquitous than we may naively expect from theory. Researchers are challenged to explain how Mars' thin atmosphere produces sufficiently strong winds to maintain active dunes[17]. And there is no consensus on the sediment composition of dunes on Titan[4] or Pluto[3], where candidate materials are either too weak or too heavy for sustained saltation. These debates suggest that our theoretical understanding of threshold and collision dynamics of wind-blown sediments are incomplete.

It has long been recognized that there are two thresholds for wind-blown transport[1]: The 'fluid' threshold is the wind required to move a particle from rest, and the 'impact' threshold is the minimum wind to maintain steady saltation. Mass transport scales in excess of the latter, whereas saltation must start from the former[7]. In this Article we offer novel theories for these two thresholds and apply them to six planetary bodies known to have aeolian features in our
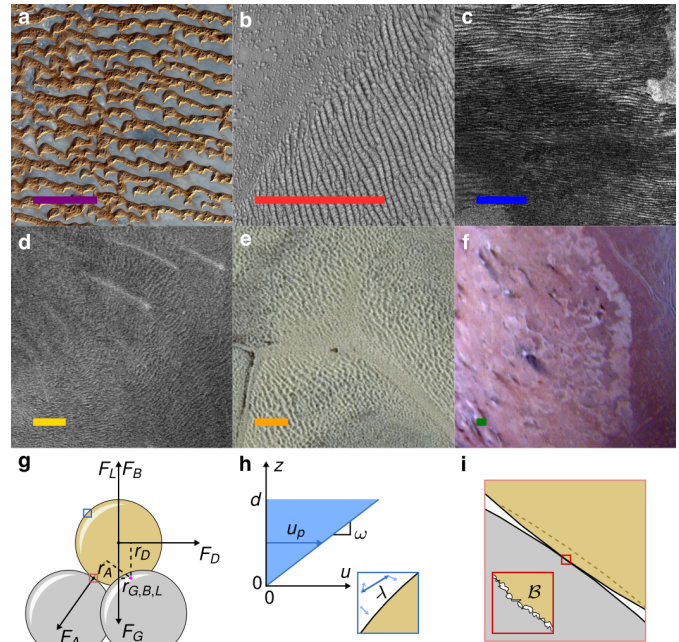
Figure 1. Dunes and the forces that create them. Aeolian features on **(a)** Earth, **(b)** Mars, **(c)** Titan, **(d)** Venus, **(e)** Pluto and **(f)** Triton. Image credit for **(a–f)** is given in Table S1, scalebars are 10 km. **(g)** The forces (F) and moments (r) of lift (L), buoyancy (B), drag (D), gravity (G) and adhesion (A) around the pivot (magenta dot) for the fluid threshold of the yellow particle. **(h)** Graphical definitions of fluid velocity (u), elevation (z), vorticity (ω), particle diameter (d), fluid velocity at the particle center elevation (u_p), with a close-up of the blue inset in **(g)** showing the mean free path of gas molecules (λ). **(i)** Close-up of the pink inset in **(g)** of a particle contact and microscopic roughness characterized by $\mathcal{B}$.

Solar System (Fig. 1a-f). We do this from first principles, and by employing more stringent or recent results from aeronautics and contact mechanics that are not typically considered in aeolian studies. Each theory has a single physically-meaningful free parameter, which are found by fitting to a newly compiled comprehensive data set. Using these theories, we provide revised predictions of the thresholds across the Solar System, paying special attention to the range of environmental conditions on each planetary body. Finally, we use a measure of attrition susceptibility of minerals at threshold to assess the likelihood and potential origins of candidate dune sands.

Fluid threshold

The fluid threshold of motion is defined by a balance between the forces retaining a grain that is resting in a pocket on a bed of grains, and the forces that can remove it from that pocket[8]. Weight and adhesion forces correspond to the former, while drag and buoyancy to the latter. The lift force can act to retain or remove the grain, depending on shear and fluid properties (Fig. 1h), but it is typically small compared to the other forces. These forces all have functional forms constrained from theory, aside from the lift and drag forces where we employ refined empirical predictions for the respective coefficients. The complete torque balance in a fragile pocket geometry reads $r_G F_G + r_A F_A = r_D F_D + r_L F_L + r_B F_B$, where the moments and forces are defined graphically in Figure 1g. Expanding and non-dimensionalizing this equation (Methods M1), we can write the fluid threshold of motion as the sum of two fractions that equal unity,

$$1 = \frac{\alpha}{\Theta_p} + \frac{\beta}{\Phi_p}, \tag{1}$$

where α and β depend on geometry and the drag and lift coefficients, and Θ_p and Φ_p depend on fluid and solid properties. The Shields-like number $\Theta_p \propto 1/d$ non-dimensionalizes the fluid speed at the particle centre, u_p, using the submerged particle weight, whereas u_p is non-dimensionalized in the parameter $\Phi_p \propto d$ by the adhesion due to grain-surface energy, γ (Methods M2). Noting the scaling of these parameters with grain diameter, d, it is clear that for small particles the threshold tends toward $\Phi_p = \beta$, and for large particles, $\Theta_p = \alpha$. The cross-over between these limiting behaviors, where winds must overcome adhesion or weight, respectively, depends on all parameters. As an example, for typical quartz grains on Earth this transition occurs for a grain size of roughly 40 μm; hence, dune sands are little affected by adhesion, while dust grains are strongly affected. This may not, however, generally be the case on other planets.

Importantly, there is one unaccounted-for constant required to close the solution for the fluid threshold described above; the ratio of the characteristic length-scales between particles in contact, d_0, and roughness at the contact scale[13] (Fig. 1i). Assuming that this ratio, $\mathcal{B}$, is approximately universal for natural sand grains, we determine its value to be $\mathcal{B} \approx 8.74$ by fitting the theory to wind-tunnel and field measurements of the fluid threshold (Methods M3). This allows prediction of the fluid threshold on each planetary body of interest, if the dimensionless parameters α, β, Θ_p, and Φ_p are known. Our formulation builds on previous hydrodynamic approaches[8,18] (Text S1), with the following improvements: it accounts for the lift and adhesion forces explicitly, improves the paramaterizations for the lift and drag coefficients[11,19], and has just one free parameter that is specific to sediment transport.

Using well-established theory on the behavior of gases[12] (Methods M4), observations of temperature and pressure, and measured material constants (Table ED1), we find that the predicted fluid entrainment threshold spans three orders of magnitude for reasonable grain diameters across the Solar System (Fig. 2a). To first order, this range is controlled by fluid kinematic viscosity (Fig. ED1). We see that both particle composition, and variability in pressure and temperature, can lead to a wide range of threshold wind speeds on a given planetary body — with the exception of Earth, where these parameters vary little. These predictions are mostly higher than alternative theories[8,9], while being similarly accurate when compared to experimental data (Figs. ED2 & ED3). We also note that the sensitivity of the drag pressure to the wind stress — i.e., the drag coefficient, C_D — varies greatly across these environments, depending on how rarefied and fast the fluid is[11] (Fig. 2b,e,f). This broad swath in fluid properties is mostly captured by pressure-controlled experiments, with the exception of small bodies that maintain very thin atmospheres such as Triton. There is a distinct lack of experimental data where adhesion dominates the fluid threshold, and where the threshold is extremely high (Fig. 2c,d).

Impact threshold

Once wind exceeds the fluid threshold, saltation is initiated. At this point the mechanism for threshold changes qualitatively: the dominant way in which grains leave the bed is by ejection due to impact from colliding grains[1]. The forces used in the fluid threshold above, aside from adhesion, also describe the physics of saltating grain trajectories (Methods M5). Interestingly, there are two approximately universal characteristics about these trajectories: saltators eject from the bed at an approximately fixed angle; and typically only one saltator is ejected per impact, while other grains 'splash' short distances and quickly deposit[20,21]. If we couple trajectory dynamics with a model for the speed ratio between the impacting ($v_\downarrow$) and ejecting ($v_\uparrow$) saltators — i.e.,
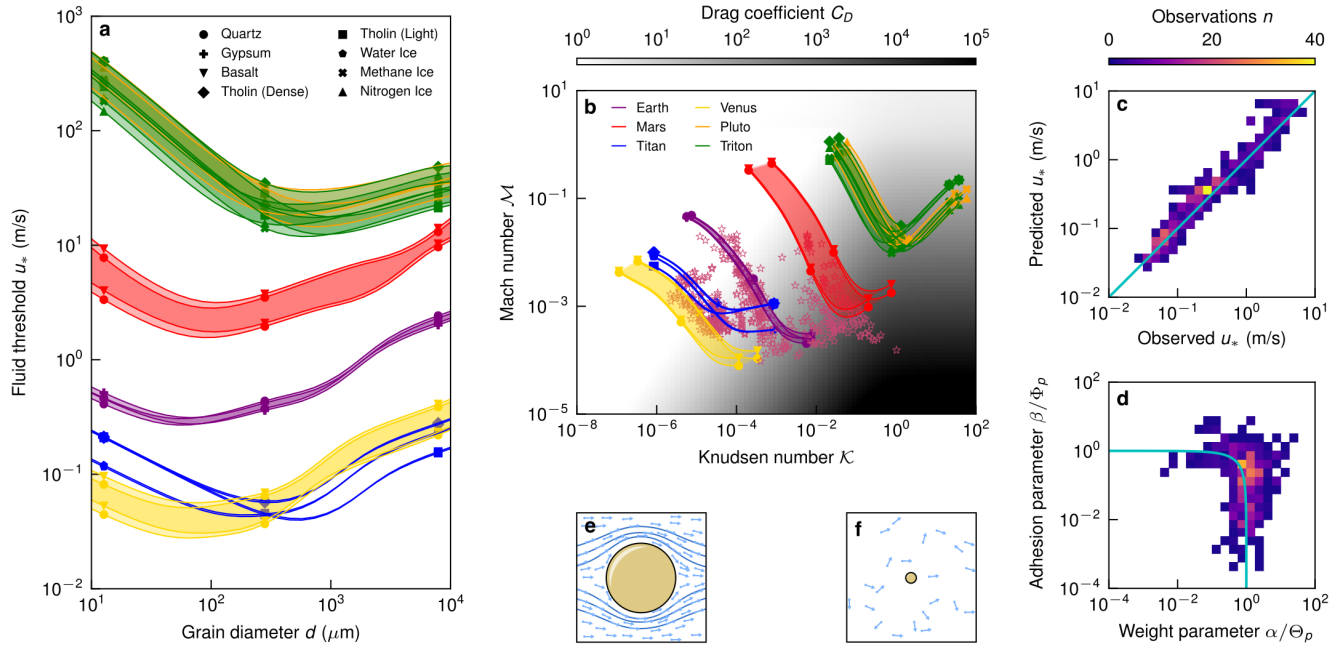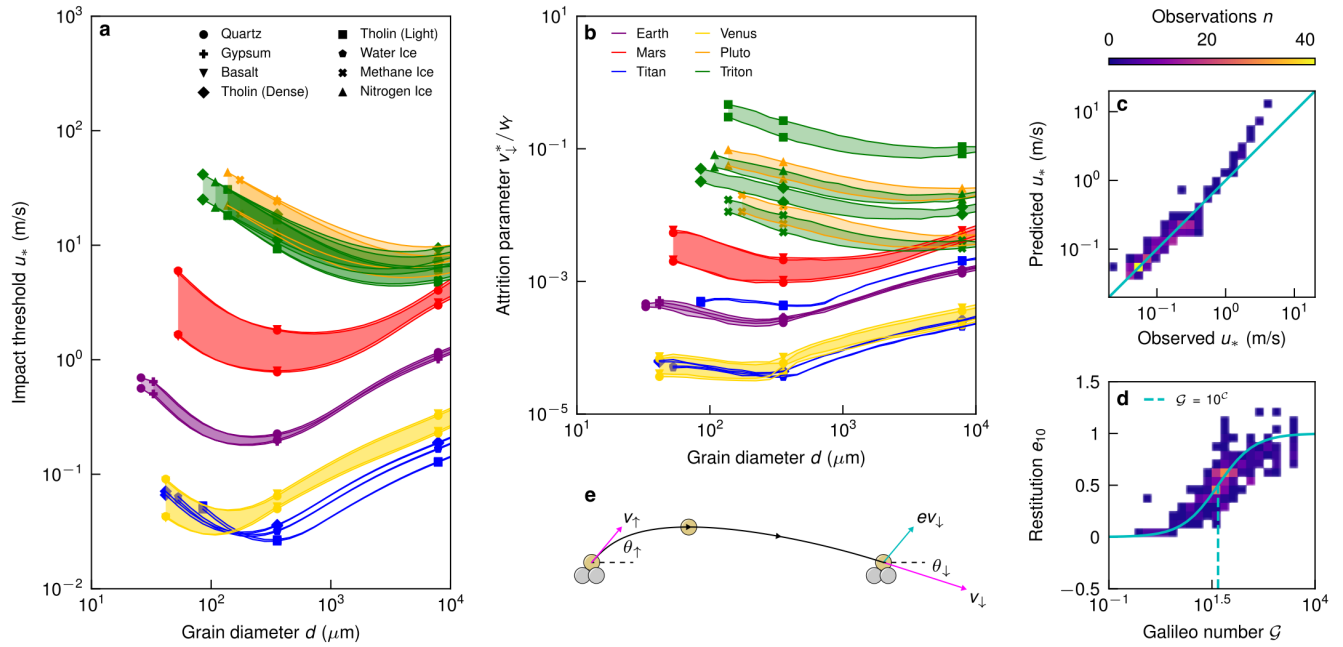
Figure 2. Fluid threshold prediction and observations. (a) Predicted fluid threshold friction velocities for grains of different candidate and known minerals, on each planetary body (legend for the latter in **b**. **(b)** Fluid regime cast in Knudsen ($\mathcal{K}$) and Mach ($\mathcal{M}$) number space for predictions (bands) and observations (stars) at the fluid threshold; background greyscale gradient indicates drag coefficient (C_D). Bands in **(a)** and **(b)** show the range based on known temperature and pressure variability. **(c)** Histogram comparing observed fluid thresholds and their predicted value; a 1:1 line (cyan) is overlaid. **(d)** Equation 1 (cyan) overlaid on a histogram of observations. **(e)-(f)** Schematics of the continuum and free-molecular limits corresponding to $\mathcal{K}$ above them, respectively.

the effective restitution coefficient e — we can find the minimum friction velocity necessary to maintain a steady-state, $v_\uparrow = e v_\downarrow$ (Fig. 3e). This state corresponds to a balance between the momentum lost during a collision to the granular bed and viscous dissipation, and momentum gained by fluid drag and lift during the hop[22].

Our effective restitution coefficient includes contributions from particle elasticity, granular friction and viscous dissipation[10,21,23]. It may be back-calculated from experimental and field studies of the impact threshold, by solving for trajectories at the conditions threshold was measured (Text S2). We seek an intuitive and parsimonious parameterization for e. Drawing on studies showing that e depends on a competition between particle inertia and viscous dissipation[21,23], we assume that other contributions vary little among materials. To test this idea we examine the relation between e_{10}, the restitution coefficient associated with a fixed common impact angle of $-10°$, and the Galileo number, $\mathcal{G} = \sqrt{(\rho_s/\rho_f - 1)gd^3}/\nu$, which has been identified as an important parameter governing sediment transport[6,24] (Figs. 3d & ED6). The resulting correlation is strong; we suggest a heuristic logistic functional form for $e_{10}(\mathcal{G})$, where the only free parameter $e_{10}(\mathcal{G} = 10^\mathcal{C}) = 1/2$ defines the crossover from the end-member cases of a fully-damped and fully-elastic impact event (Methods M6). By fitting to observations we find $\mathcal{C} \approx 1.65$ (Fig. 3c,d), which can be implemented in a forward model to predict the impact threshold. This theory builds on previous contributions[7,22]; the main improvements are that forces are represented more accurately, and that the number of free parameters is reduced because the ejection speed of grains does not need to be prescribed.

We find that computed impact thresholds cover a span in magnitude that is comparable to the fluid thresholds, with the latter exceeding the former in nearly all cases — likely leading to hysteresis in sediment transport events[5] (Fig. 3a). Compared to previous theories[5–7] our approach is more accurate when compared to observations, and predicts lower impact thresholds in less dense fluids (Figs. ED4 & ED5). Notably, our formulation of the impact threshold becomes ill-defined for small grain sizes (Fig. ED8, Methods M5). This occurs approximately where the two thresholds reach parity, and where turbulent fluctuations — neglected in our Reynolds-averaged description — are expected to become important in determining grain trajectories. While alternative methods avoid this pathology by imposing that the impact threshold smoothly approaches the fluid one in this limit[25], we note that there is a distinct lack of data to test ideas about small grains.

Our theory permits us to resolve characteristic saltator trajectories, and therefore the impact speed (Figs. ED7 & ED9). This characterizes the energy that results in wind-driven sediment attrition, a critical mechanism in wearing down particles

Figure 3. Impact threshold prediction and observations. (a) Predicted impact threshold friction velocities for grains of different candidate and known minerals on each planetary body. Legends follow Figure 2. **(b)** Predicted attrition of characteristic particles at the impact threshold. Bands in **(a)** and **(b)** show the ranges for each planet based on known temperature and pressure variability. **(c)** Histogram comparing observed impact thresholds and their predicted value, a 1:1 line (cyan) is overlaid. **(d)** Heuristic $e_{10}(\mathcal{G})$ (cyan) overlaid on a histogram of observations, dashed line (cyan) defines the fit-parameter $\mathcal{C}$. **(e)** Trajectory at the impact threshold for 100 μm Basalt on Venus (grains, path and vectors are consistently scaled).

and potentially producing dust[26–28]. By employing a canonical model for yield during particle impact[10], using the material properties of sediment mineral candidates (Methods M7), we inspect the ratio of the impact speed at threshold over the speed required to cause yield, $v_{\downarrow}^*/v_Y$ (Fig. 3b). This constitutes an attrition parameter; if this ratio is very small, relatively strong sediment particles were likely produced from weathering rather than attrition of bedrock, whereas large values would indicate weak particles that could not survive impact and make dunes. To build intuition regarding what numerical values for $v_{\downarrow}^*/v_Y$ mean, we compute them for two representative materials on Earth — quartz, and gypsum. While the former is stronger than the latter, both form competent sand grains that round — rather than shatter — when transported by wind[26,28]. Gypsum, however exhibits significant attrition over just several kilometers of transport, while quartz requires an order of magnitude larger distance; their corresponding values for $v_{\downarrow}^*/v_Y$ differ by roughly 50%. Turning to other planetary bodies, we see striking variability in the attrition susceptibility of candidate dune sands across the Solar System. Curiously, the slope of the attrition parameter with grain size does not have a consistent sign across environments. We speculate that negative slopes imply efficient production of dust, if there is equal transport susceptibility of grain-sizes[29].

Implications

In this study we have highlighted how the large variation in atmospheric conditions and particle properties on each planetary body leads to markedly different aeolian sediment transport thresholds. To achieve this we have employed better representation of the mechanisms that change substantially outside Earth. Indeed, the minimal effect of environmental and mineral variability on Earth's thresholds is a red herring; these play major roles in all other bodies we study (Fig. 2a). Of course, there are mechanisms known to play a role in the saltation threshold that we have not represented here; notably, capillary[30] and electrostatic forces[31]. Our analysis, however, has revealed that there are potentially important and previously unconsidered mechanisms that we do not currently understand — like lift at low pressure (Text S3), and the fluid threshold in the adhesion limit (Fig. 2d). We also note that we do not explicitly account for adhesion effects in the impact threshold theory; some results indicate that adhesion may be neglected for saltation[24].

This work may help to resolve some unsettled debates in planetary aeolian geomorphology. For Pluto, our analysis supports the hypothesis that Methane ice constitutes the dunes west of Sputnik Planitia[3]. The dark streaks on Triton are likely inactive

after plume deposition, due to high entrainment thresholds and erosion susceptibility[32,33]. Venusian sands are likely sourced by non-aeolian mechanisms, and transport has negligible hysteresis akin to water on Earth[7]. On Titan, more work is needed to understand the aggregation and attrition of Tholins, but our results support locally-sourced and low-density Tholin dune sands[4,34]. Finally, on Mars we suggest that sand grains observed by Curiosity actively produce dust through attrition[35], and require stronger winds to move than GCMs predict[17] – perhaps through katabatics[36] or strong instability in the boundary layer[16].

References

1. Bagnold, R. A. *The physics of blown sand and desert dunes* (Courier Corporation, 1941).

2. Hayes, A. G. Dunes across the solar system. *Science* **360**, 960–961 (2018).

3. Telfer, M. W. *et al.* Dunes on pluto. *Science* **360**, 992–997 (2018).

4. Yu, X., Hörst, S. M., He, C., McGuiggan, P. & Crawford, B. Where does titan sand come from: insight from mechanical properties of titan sand candidates. *J. Geophys. Res. Planets* **123**, 2310–2321 (2018).

5. Kok, J. F. An improved parameterization of wind-blown sand flux on mars that includes the effect of hysteresis. *Geophys. Res. Lett.* **37** (2010).

6. Pähtz, T. & Durán, O. The cessation threshold of nonsuspended sediment transport across aeolian and fluvial environments. *J. Geophys. Res. Earth Surf.* **123**, 1638–1666 (2018).

7. Claudin, P. & Andreotti, B. A scaling law for aeolian dunes on mars, venus, earth, and for subaqueous ripples. *Earth Planet. Sci. Lett.* **252**, 30–44 (2006).

8. Shao, Y. & Lu, H. A simple expression for wind erosion threshold friction velocity. *J. Geophys. Res. Atmospheres* **105**, 22437–22443 (2000).

9. Iversen, J. D. & White, B. R. Saltation threshold on earth, mars and venus. *Sedimentology* **29**, 111–119 (1982).

10. Johnson, K. L. *Contact mechanics* (Cambridge university press, 1987).

11. Loth, E. Compressibility and rarefaction effects on drag of a spherical particle. *AIAA J.* **46**, 2219–2228 (2008).

12. Byron Bird, R. Transport phenomena. *Appl. Mech. Rev.* **55**, R1–R4 (2002).

13. Israelachvili, J. N. *Intermolecular and surface forces* (Academic press, 2011).

14. Swann, C., Sherman, D. & Ewing, R. Experimentally-derived thresholds for windblown sand on mars. *Geophys. Res. Lett.* (2019).

15. Jerolmack, D. J. & Brzinski III, T. A. Equivalence of abrupt grain-size transitions in alluvial rivers and eolian sand seas: A hypothesis. *Geology* **38**, 719–722 (2010).

16. Gunn, A. *et al.* Circadian rhythm of dune-field activity. *arXiv preprint arXiv:1812.03612* (2018).

17. Banfield, D. *et al.* The atmosphere of mars as observed by insight. *Nat. Geosci.* 1–9 (2020).

18. Wiberg, P. L. & Smith, J. D. Calculations of the critical shear stress for motion of uniform and heterogeneous sediments. *Water resources research* **23**, 1471–1480 (1987).

19. Loth, E. Lift of a spherical particle subject to vorticity and/or spin. *AIAA J.* **46**, 801–809 (2008).

20. Anderson, R. S. & Haff, P. K. Simulation of eolian saltation. *Science* **241**, 820–823 (1988).

21. Beladjine, D., Ammi, M., Oger, L. & Valance, A. Collision process between an incident bead and a three-dimensional granular packing. *Phys. Rev. E* **75**, 061305 (2007).

22. Andreotti, B. A two-species model of aeolian sand transport. *J. Fluid Mech.* **510**, 47–70 (2004).

23. Gondret, P., Lance, M. & Petit, L. Bouncing motion of spherical particles in fluids. *Phys. fluids* **14**, 643–652 (2002).

24. Pähtz, T. & Durán, O. Unification of aeolian and fluvial sediment transport rate from granular physics. *Phys. Rev. Lett.* **124**, 168001 (2020).

25. Durán, O., Claudin, P. & Andreotti, B. On aeolian transport: Grain-scale interactions, dynamical mechanisms and scaling laws. *Aeolian Res.* **3**, 243–270 (2011).

26. Jerolmack, D. J., Reitz, M. D. & Martin, R. L. Sorting out abrasion in a gypsum dune field. *J. Geophys. Res. Earth Surf.* **116** (2011).

27. Ghadiri, M. & Zhang, Z. Impact attrition of particulate solids. part 1: A theoretical model of chipping. *Chem. Eng. Sci.* **57**, 3659–3669 (2002).

28. Crouvi, O., Amit, R., Enzel, Y., Porat, N. & Sandler, A. Sand dunes as a major proximal dust source for late pleistocene loess in the negev desert, israel. *Quat. Res.* **70**, 275–282 (2008).

29. Martin, R. L. & Kok, J. F. Size-independent susceptibility to transport in aeolian saltation. *J. Geophys. Res. Earth Surf.* **124**, 1658–1674 (2019).

30. McKenna Neuman, C. & Sanderson, S. Humidity control of particle emissions in aeolian systems. *J. Geophys. Res. Earth Surf.* **113** (2008).

31. Kok, J. F. & Renno, N. O. Electrostatics in wind-blown sand. *Phys. Rev. Lett.* **100**, 014501 (2008).

32. Sagan, C. & Chyba, C. Triton's streaks as windblown dust. *Nature* **346**, 546–548 (1990).

33. Hansen, C., McEwen, A. S., Ingersoll, A. & Terrile, R. Surface and airborne evidence for plumes and winds on triton. *Science* **250**, 421–424 (1990).

34. Burr, D. M. *et al.* Higher-than-predicted saltation threshold wind speeds on titan. *Nature* **517**, 60–63 (2015).

35. Weitz, C. M. *et al.* Sand grain sizes and shapes in eolian bedforms at gale crater, mars. *Geophys. Res. Lett.* **45**, 9471–9479 (2018).

36. Ewing, R. C., Peyret, A.-P. B., Kocurek, G. & Bourke, M. Dune field pattern formation and recent transporting winds in the olympia undae dune field, north polar region of mars. *J. Geophys. Res. Planets* **115** (2010).

37. Gondret, P., Hallouin, E., Lance, M. & Petit, L. Experiments on the motion of a solid sphere toward a wall: From viscous dissipation to elastohydrodynamic bouncing. *Phys. Fluids* **11**, 2803–2805 (1999).

Data & code availability
All data is available in the Tables ED1, S2, S3, S4 and S5. Code to reproduce this paper can be found at `https://github.com/algunn/solar-system-saltation`.

Author contributions
Conceptualization, Data Curation, Formal Analysis, Investigation, Software, Validation, Visualization, Writing – original draft, A.G.; Methodology, Project Administration, Writing – review & editing, A.G. and D.J.J.; Resources, Funding Acquisition, Supervision, D.J.J.

Competing interests
The authors declare no competing interests.

Materials & Correspondence
All correspondence should be directed to Douglas Jerolmack (sediment@sas.upenn.edu).

Methods

M1 Fluid threshold theory

The schematic in Figure 1g shows the convention of the force directions and the exact pocket geometry we use. The three-dimensional pocket is created by particles of equal diameter, lying in a horizontal plane in an equilateral triangle. The moments are exact for spheres, and the pivot can be thought of as a line between the contacts of the two bed particles downwind of the

threshold particle. The forces (F), moments (r), and torque balance read,

$$F_A = \frac{\pi}{2}\gamma d e^{-\mathcal{B}}, \qquad \frac{r_A}{d} = \frac{1}{2\sqrt{2}},$$

$$F_D = \frac{\pi}{8}C_D\rho_f d^2 u_p^2, \qquad \frac{r_D}{d} = \frac{1}{\sqrt{6}},$$

$$F_L = \frac{\pi}{8}C_L\rho_f d^2 u_p^2, \qquad \frac{r_L}{d} = \frac{1}{4\sqrt{3}}, \qquad\qquad r_G F_G + r_A F_A = \mathcal{A}(r_D F_D + r_L F_L) + r_B F_B,$$

$$F_B = \frac{\pi}{6}g\rho_f d^3, \qquad \frac{r_B}{d} = \frac{1}{4\sqrt{3}},$$

$$F_G = \frac{\pi}{6}g\rho_s d^3, \qquad \frac{r_G}{d} = \frac{1}{4\sqrt{3}},$$

where subscripts A, D, L, B and G, correspond to adhesion, drag, lift, buoyancy and gravity respectively. γ is the surface energy, d is the grain diameter, $\mathcal{B}$ is the ratio of contact-scale roughness to the inter-particle distance in contact[13], C_D is the drag coefficient, ρ_f is the fluid density, u_p is the horizontal flow speed at the particle center, C_L is the lift coefficient, ρ_s is the solid density, and $\mathcal{A}$ is the ratio of a sphere's frontal area to natural sediment effective frontal area with respect to the flow for drag and lift. Equation 1 is the information above rearranged into a compact and meaningful form, where we have employed accurate ways to model each parameter if need be. Substituting the forces and moments into the torque balance, we can write,

$$u_p^2 = \frac{1}{2\sqrt{2}C_D + C_L}\frac{4}{3}\left(\frac{gd(s-1)}{\mathcal{A}} + 3\sqrt{6}\frac{\gamma e^{-\mathcal{B}}}{d\rho_f \mathcal{A}}\right),$$

where s is the ratio of the solid to fluid densities, ρ_s/ρ_f. Now dividing by the left-hand-side and defining α, β, Θ_p and Φ_p we arrive at Equation 1 in the main text,

$$\alpha = \frac{1}{2\sqrt{2}C_D + C_L}\frac{4}{3\mathcal{A}},$$

$$\beta = \frac{1}{2\sqrt{2}C_D + C_L}\frac{4\sqrt{6}e^{-\mathcal{B}}}{\mathcal{A}},$$

$$\Theta_p = \frac{u_p^2}{gd(s-1)},$$

$$\Phi_p = \frac{u_p^2 d\rho_f}{\gamma},$$

$$1 = \frac{\alpha}{\Theta_p} + \frac{\beta}{\Phi_p}.$$

We have chosen the notation for Θ_p because replacing u_p with u_* gives the Shields number Θ; Φ_p follows suit. All the parameters in α and β are dimensionless, and they encode information about shape and sensitivity. All the parameters in Θ_p and Φ_p are dimensional, and these encode the system state. If the sum of fractions in Equation 1 is greater than one, the state is below the fluid threshold.

In Methods M3 we find $\mathcal{A}$ and $\mathcal{B}$. In Methods M4 we find the kinematic viscosity ν (required to link u_p with u_*[M1], as explained in Text S4), ρ_f, the mean free path λ and speed of sound c; these parameters are required to find C_D and C_L using the empirical correlations we employ from Loth[11, 19]. In Methods M2 we find γ. Values and ranges for these variables, along with the fixed ones, are given in Table ED1. Finally, grain diameter (d) is the independent parameter.

M2 Surface energy theory

The adhesion force between particles depends linearly on the surface energy, γ. Ideally γ is measured, typically in the correct geometry and environment with an AFM. Without this ability, we employ the Lifshitz theory to estimate the Hamaker constant, A[13]. For two perfect like spheres, A and γ are coupled so that,

$$\gamma = \frac{A}{12\pi d_0^2},$$

where $d_0 = 0.165$ nm is the characteristic distance between particles in contact[13]. Lifshitz theory takes information about the solids in contact and the gas they are immersed in, and provides an approximation for the Hamaker constant, A, such that,

$$A = \frac{3}{4} k_B T \left(\frac{\varepsilon_s - \varepsilon_f}{\varepsilon_s + \varepsilon_f} \right)^2 + \frac{3 \hbar v_e}{16\sqrt{2}} \frac{\left(n_s^2 - n_f^2\right)^2}{\left(n_s^2 + n_f^2\right)^{3/2}},$$

where subscripts s and f denote solid and fluid, respectively, k_B is Boltzmann's constant, T is the temperature, ε is the static relative permittivity, $\hbar$ is the reduced Plank constant, v_e is the frequency of the absorption peak (assumed to be $3 \cdot 10^{15}$ 1/s for all media) and n is the refractive index. n depends on temperature (and pressure for the gas), so over the relatively small variations we consider on each planetary body we assume a linear relationship of n constrained by known values of $n(T, p)$. This calculation is performed for all cases apart from Tholin, where γ was measured with an AFM by Yu *et al.* (2017)[M2]. While it is clear that γ depends on the environment from the equation above, in lieu of alternatives we assume to first order that the AFM measurement for Tholin holds in all cases. In Table S2 we provide referenced values for the material-specific constants used in this calculation for all other cases.

M3 Fluid threshold fit

We compiled previously measured fluid threshold friction velocities from experiments and field studies to find the unknown parameter $\mathcal{B}$[14,30,34,M3–M31]. We chose to only include measurements where the humidity was reported to be less than 15%, as to minimize the effect of capillary forces[M32]. In order to implement this fit, all the other parameters that make up Equation 1 must be known for each observation. We used the variables stated in each paper where possible. Otherwise, we assumed measurements were taken at $T = 20$ °C and standard pressure for the elevation they were measured, then made use of the equations in Methods M4 if required. All papers do not report the surface energy, γ, for their experiments; in lieu of this important parameter, we used reference Hamaker constants from measurements in other literature for each sediment material[13,M2,M33,M34] (or a similar material if a measurement could not be found, i.e. clover seed was assumed to adhere the same as walnut shells). These data are collated in Table S3.

In the main text and result we only fit using one parameter, $\mathcal{B}$; there is an additional free parameter however, $\mathcal{A}$, that in principle should depend on the sediment shape[6]. In an ideal configuration $\mathcal{A} = 1$, and when allowing it to vary freely alongside $\mathcal{B}$ to match observations we find it to be $\mathcal{A} = 1.01$. Given the similarity between these results, and the negligible effect on accuracy between them (Fig. ED2a,b), we fix $\mathcal{A} = 1$. The fitting parameters are found by minimizing,

$$\sum_{n=1}^{N} \left(\frac{u_{*,observed}}{u_{*,predicted}} - 1 \right)^2,$$

with $N = 567$ being the number of fluid threshold measurements compiled in this study. This form of the loss was used to ensure there is no bias toward the magnitude of u_*.

M4 Fluid property theory

We assume the gases can be described as ideal, with the kinetic theory of gases, and with respect to viscosity using a Lennard-Jones pair-potential between molecules. This allows us to find the fluid properties related to sediment transport using just temperature, pressure and material constants. The dynamic viscosity ($\mu = \rho_f v$) is found using the Lennard-Jones model[12],

$$
\begin{aligned}
T_* &= \frac{T k_B}{\varepsilon_T}, \\
\Omega_*^{(2,2)} &= A_T T_*^{-B_T} + C_T e^{-D_T T_*} + E_T e^{-G_T T_*}, \\
\mu &= 2.6693 \cdot 10^{-6} \frac{\sqrt{MT}}{\sigma^2 \Omega_*^{(2,2)}},
\end{aligned}
$$

where $A_T = 1.16145$, $B_T = 0.14874$, $C_T = 0.52487$, $D_T = 0.77320$, $E_T = 2.16178$ and $G_T = 2.43787$ are fit parameters for the reduced viscosity collision integral $\Omega_*^{(2,2)}$[M35]. The Boltzmann constant k_B is $1.38 \cdot 10^{-23}$ J/K. Material constants σ, ε_T and M are given in Table S2. This formulation is used, instead of the Sutherland formula employed in other sediment transport studies[3,5], because it extrapolates more reliably since it does not assume hard-sphere repulsion at short range.

Fluid density is found using the ideal gas law[12],

$$\rho_f = \frac{pM}{RT},$$

where $R = 8.314$ J/K/mol is the gas constant.

Mean free path is found using the kinetic theory of gases[12],

$$\lambda = \frac{\mu}{p}\sqrt{\frac{\pi RT}{2M}}.$$

The Mach ($\mathcal{M} = c/u_p$), Knudsen ($\mathcal{K} = \lambda/d$) and Reynolds ($\mathcal{R} = u_p d/\nu$) numbers are related by,

$$\mathcal{K} = \frac{\mathcal{M}}{\mathcal{R}}\sqrt{\frac{\pi\gamma_C}{2}},$$

where γ_C is the heat capacity ratio, a material constant given in Table ED1. This is useful when interpreting Figure 2b, as the drag coefficient (and 'crisis') is typically displayed as a function of $\mathcal{R}$.

M5 Grain trajectory theory

Grains in flight obey an equation of motion defined by the force balance,

$$m_p\frac{\partial v}{\partial t} = F_D + F_L + F_G + F_B,$$

where m_p is the particle mass, v is the particle velocity, t is time, F is force, and subscripts D, L, G and B denote drag, lift, gravity and buoyancy, respectively. Substituting the forces in Methods M1 and rearranging, we find the following equation of motion (written in the complex plane for simplicity),

$$\frac{\partial v}{\partial t} = \frac{3}{4}(C_D + iC_L)\frac{|u_p(z_p) - v|(u_p(z_p) - v)}{sd} - i\left(1 - \frac{1}{s}\right)g,$$

where $v = v_x + iv_z$ is the particle velocity vector, t is time, C_D and C_L are the drag and lift coefficients, respectively, $u_p = u_x(z_p) + 0i$ is the horizontal fluid speed at the particle center, z_p is the elevation (where zero is defined at the base of a particle at rest on the bed), $s = \rho_s/\rho_f$ is the solid to fluid density ratio, d is the grain diameter, and g is the gravity acceleration. This equation states that particles have drag, lift and effective weight altering their path as they are in flight. Drag and lift magnitude depend on the square of the relative speed of the particle with respect to the flow, as to their angles, while gravity acts constantly and always downward. Implicit in this formulation is that the particles do not extract momentum from the flow, since the formulation of u_x we employ is only effected by the roughness that grains impart on the flow[M1]. This is a common and reasonable assumption at the impact threshold[5–7], since this is the edge of the regime where there are no particles moving. Solving this equation for a grain trajectory, from ejection to impact, is an initial value problem that requires numerical integration. Position, velocity and acceleration are all present in this ordinary differential equation (ODE). We define the initial and final values of the velocity vectors as,

$$v|_{(z_p=d/2)\wedge(t=0)} = v_\uparrow e^{i\theta_\uparrow},$$
$$v|_{(z_p=d/2)\wedge(t\neq0)} = v_\downarrow e^{i\theta_\downarrow},$$

respectively, where $v_\uparrow$ is the ejection speed, $\theta_\uparrow = 50°$ is the fixed ejection angle[20,21], $v_\downarrow$ is the impact speed, and $\theta_\downarrow$ is the impact angle. For a steady-state trajectory, the relation $v_\uparrow = ev_\downarrow$ holds where e is the restitution coefficient, i.e., the ratio of momentum maintained in saltation. In Methods M6 we show how e is parameterized using $\theta_\downarrow$ and the Galileo number, $\mathcal{G}$. Clearly, since we seek a solution to an ODE where the target initial value must be chosen as a function of the final value, we must not only numerically integrate the initial value problem, but also iteratively converge on the steady-state solution. Please see the 'Data & code availability' statement for our approach to this problem implemented using SciPy[M36].

In Figure ED7 it is clear that there are multiple pairs of u_* and $v_\uparrow$ such that $v_\uparrow = ev_\downarrow$; however we seek a unique pair that defines the impact threshold. We require the minimum friction velocity for which this equality holds. Inspecting a well-posed case (Figs. ED7 & ED8a), for each curve of fixed friction velocity, all ejection speeds aside from the solution result in the ratio of the ejection to impact speeds being too large — i.e. the particles do not gain enough momentum during flight to sustain transport. Coupling these two critical ideas, we define the impact threshold friction velocity as the one that produces a trajectory such that the ratio of ejection to impact speed (normalized by impact angle, see Methods M6) is equal to the restitution coefficient corresponding to the system's Galileo number. Solving for this case requires a third layer of numerical methods that is implemented in our public code.

M6 Restitution parameterization

To find a restitution coefficient (e) parameterization, we compiled previously measured impact threshold friction velocities from experiments and field studies[M4–M6, M22, M27, M37–M43]. As noted in the main text, this choice of parameterization requires a single fit parameter, $\mathcal{C}$. In order to find $\mathcal{C}$, all the other parameters that make up the trajectory equation of motion (Methods M5) must be known for each observation. Like the fluid threshold measurements, we used the variables stated in the paper where possible. Otherwise, we assumed measurements were taken at $T = 20\,°C$ and standard pressure for the elevation they were measured, then made use of the equations in Methods M4 if required. These data are collated in Table S4. With these known, we calculate $v_\uparrow/v_\downarrow$ and $\theta_\downarrow$ for each measurement using the observed u_*; our theory for e should ideally be equal to $v_\uparrow/v_\downarrow$ for each measurement.

We also compiled data from other studies where the restitution coefficient of particles hitting a loose bed was explicitly measured[20, 21, M44–M49]. If these measurements were from studies where wind was blowing particles, we only considered the measurements at the impact threshold. This distinction is important since the bulk restitution will be altered by particles extracting momentum from the flow and bed particles not being at rest. As above, we used the variables stated in the paper where possible. Otherwise, we assumed measurements were taken at $T = 20\,°C$ and standard pressure for the elevation they were measured, then made use of the equations in Methods M4 if required. These data are collated in Table S5. It is clear from one of these studies[21] that a good approximation for the effect of impact angle on restitution — also employed elsewhere — is[M50],

$$\frac{e}{e_{10}} = \frac{1 - e_\alpha \sin(\theta_\downarrow)}{1 - e_\alpha \sin(10)},$$

where e_{10} is the restitution coefficient when $\theta_\downarrow = -10°$ and $e_\alpha \approx 0.828$ is found experimentally[21]. We choose $10°$ arbitrarily, but require that all restitution coefficients are normalized as if they are found from equal impact angles when trying to derive a parameterization.

Relevant studies indicate that the restitution coefficient of saltators is independent of impact speed[20, 21, M44, M48, M49, M51, M52]. This contrasts with restitution coefficient of a single particle impacting a plane, which increases with impact speed after a threshold and is predictive using the Stokes number[37, M53]. For the narrowly-defined restitution coefficient we attempt to accurately model, we are interested in non-unique saltators in the limit of vanishing sediment flux during events where a loose bed also produces splash. In this case, we seek a non-dimensional parameter that does not include a velocity scale, that clearly relates to the restitution coefficient from experiments. Guided by the trend for both explicit and implicit data (Fig. ED6c), we suggest to first order that

$$e_{10} = \frac{\mathcal{G}}{10^{\mathcal{C}} + \mathcal{G}},$$

where $\mathcal{G} = \sqrt{(s-1)gd^3}/\nu$ is the Galileo number and $\mathcal{C}$ is the fit parameter for the impact threshold. We find $\mathcal{C} \approx 1.65$ using a least-square regression onto the data described above. This approach assumes imperfectly that the restitution coefficient could potentially reach unreasonably high values (such that saltation would sustain without fluid flow, i.e. $e > 1$) if both $\mathcal{G}$ and $\theta_\downarrow$ are large. In lieu of a more appropriate data-informed alternative, however, we use the accurate formulation above, noting that our predictions lie well outside those unreasonable regimes. This formulation is consistent with intuition (as described in the main text) and data where available[M48] (Fig. ED6).

M7 Yield speed theory

We assume that the yield speed (v_Y) for two like-spheres is modeled by[10],

$$v_Y = \sqrt{\frac{26Y^5}{E_*^4 \rho_s}},$$

where Y is the yield stress, $E_* = E/2(1-V^2)$ is the effective elastic modulus (E), V is the Poisson ratio (upper-case here to avoid confusion with the particle speed used elsewhere in this manuscript) and ρ_s is the solid density. This formulation is based on the Von Mises criterion that solids yield when the maximum pressure exerted at the contact exceeds $1.6Y$. The yield stress is not necessarily related to the elastic modulus in the same way for all materials; in lieu of yield stress data for all materials used in this study, however, for geologically-relevant materials the following three semi-empirical relationships are relatively

accurate:

$$\frac{H}{Y} = 0.19 + 1.6 \log_{10} \left(\frac{E}{Y} \tan(\beta_I) \right),$$

$$H = 2 \cdot 10^{-5} E^{4/3},$$

$$\frac{E}{E_0} = \frac{2T_m - T}{2T_m - T_0},$$

from Evans & Goetze (1979)[M54], Yu *et al.* (2018)[4] and Courtney (2005)[M55], respectively, where H is the hardness measured with a nano-indentor of angle β_I, $E_0(T_0)$ is the elastic modulus measured at temperature T_0 and T_m is the melting temperature. We note that it would be ideal to use a theory on chipping of geologic materials over this approach, but current theories require measurements of fracture toughness that have not been taken for material and environments applicable to this study[27,M56]. In the special case of 'Tholin (light)', we crudely assume that the yield stress (Y_{TL}) is related to the yield stress of 'Tholin (dense)' (Y_{TD}) by the ratio of their densities, such that $Y_{TL}/Y_{TD} = \rho_{TL}/\rho_{TD}$, since the yield stress should decrease with aggregate density and experimental evidence is not available. We treat this yield speed as a characteristic value of attrition, instead of a robust predictor.

References

[M1] Guo, J. & Julien, P. Y. Buffer law and transitional roughness effect in turbulent open-channel flows. *Civ. Eng. Fac. Publ.* 5 (2007).

[M2] Yu, X., Hörst, S. M., He, C., McGuiggan, P. & Bridges, N. T. Direct measurement of interparticle forces of titan aerosol analogs ("tholin") using atomic force microscopy. *J. Geophys. Res. Planets* **122**, 2610–2622 (2017).

[M3] Baas, A. C. & Sherman, D. J. Spatiotemporal variability of aeolian sand transport in a coastal dune environment. *J. Coast. Res.* 1198–1205 (2006).

[M4] Bagnold, R. A. The size-garding of sand by wind. *Proc. Royal Soc. London. Ser. A-Mathematical Phys. Sci.* **163**, 250–264 (1937).

[M5] Burr, D. M. *et al.* A wind tunnel study of the effect of intermediate density ratio on saltation threshold. *Aeolian Res.* **45**, 100601 (2020).

[M6] Chepil, W. Dynamics of wind erosion: Ii. initiation of soil movement. *Soil Sci.* **60**, 397 (1945).

[M7] Chepil, W. Properties of soil which influence wind erosion: Iv. state of dry aggregate structure. *Soil Sci.* **72**, 387–402 (1951).

[M8] Del Bello, E. *et al.* Experimental simulations of volcanic ash resuspension by wind under the effects of atmospheric humidity. *Sci. reports* **8**, 1–11 (2018).

[M9] Dong, Z., Liu, X., Wang, H. & Wang, X. Aeolian sand transport: a wind tunnel model. *Sedimentary Geol.* **161**, 71–83 (2003).

[M10] Fletcher, B. The incipient motion of granular materials. *J. Phys. D: Appl. Phys.* **9**, 2471 (1976).

[M11] Greeley, R., Iversen, J., Pollack, J., Udovich, N. & White, B. Wind tunnel studies of martian aeolian processes. *Proc. Royal Soc. London. A. Math. Phys. Sci.* **341**, 331–360 (1974).

[M12] Greeley, R., White, B., Leach, R., Iversen, J. & Pollack, J. Mars: Wind friction speeds for particle movement. *Geophys. Res. Lett.* **3**, 417–420 (1976).

[M13] Greeley, R., Leach, R., White, B., Iversen, J. & Pollack, J. Threshold windspeeds for sand on mars: Wind tunnel simulations. *Geophys. Res. Lett.* **7**, 121–124 (1980).

[M14] Greeley, R. *et al.* Windblown sand on venus: Preliminary results of laboratory simulations. *Icarus* **57**, 112–124 (1984).

[M15] Hong, C., Xueyong, Z., Chenchen, L., Jiajia, H. & Yongqiu, W. Transport mass of creeping sand grains and their movement velocities. *J. Geophys. Res. Atmospheres* **118**, 6374–6382 (2013).

[M16] Horikawa, K., Shen, H. W. *et al.* Sand movement by wind action:(on the characteristics of sand traps). (1960).

[M17] Iversen, J. D. & Rasmussen, K. R. The effect of surface slope on saltation threshold. *Sedimentology* **41**, 721–728 (1994).

[M18] Iversen, J., Pollack, J. B., Greeley, R. & White, B. R. Saltation threshold on mars: The effect of interparticle force, surface roughness, and low atmospheric density. *Icarus* **29**, 381–393 (1976).

[M19] Kadib, A. A function for sand movement by wind. Tech. Rep., University of California, Berkeley, Institute of Engineering Research (1965).

[M20] Li, B. & McKenna Neuman, C. Boundary-layer turbulence characteristics during aeolian saltation. *Geophys. research letters* **39** (2012).

[M21] Marshall, J. R. & Greeley, R. An experimental study of aeolian structures on venus. *J. Geophys. Res. Planets* **97**, 1007–1016 (1992).

[M22] Martin, R. L. & Kok, J. F. Wind-invariant saltation heights imply linear scaling of aeolian saltation flux with shear stress. *Sci. advances* **3**, e1602569 (2017).

[M23] McKenna-Neuman, C. & Nickling, W. A theoretical and wind tunnel investigation of the effect of capillary water on the entrainment of sediment by wind. *Can. J. Soil Sci.* **69**, 79–96 (1989).

[M24] Merrison, J., Jensen, J., Kinch, K., Mugford, R. & Nørnberg, P. The electrical properties of mars analogue dust. *Planet. Space Sci.* **52**, 279–290 (2004).

[M25] Nalpanis, P., Hunt, J. & Barrett, C. Saltating particles over flat beds. *J. Fluid Mech.* **251**, 661–685 (1993).

[M26] Nickling, W. The stabilizing role of bonding agents on the entrainment of sediment by wind. *Sedimentology* **31**, 111–117 (1984).

[M27] Selah, A. & Fryrear, D. Threshold wind velocities of wet soils as affected by wind blown sand. *Soil Sci.* **160**, 304–309 (1995).

[M28] Shao, Y. & Mikami, M. Heterogeneous saltation: Theory, observation and comparison. *Boundary-layer meteorology* **115**, 359–379 (2005).

[M29] Svasek, J. & Terwindt, J. Measurements of sand transport by wind on a natural beach. *Sedimentology* **21**, 311–322 (1974).

[M30] Williams, J. J., Butterfield, G. R. & Clark, D. G. Aerodynamic entrainment threshold: effects of boundary layer flow conditions. *Sedimentology* **41**, 309–328 (1994).

[M31] Williams, J. J. *Aeolian entrainment thresholds in a developing boundary layer*. Ph.D. thesis, Queen Mary University of London (1986).

[M32] Seiphoori, A., Ma, X.-g., Arratia, P. E. & Jerolmack, D. J. Formation of stable aggregates by fluid-assembled solid bridges. *Proc. Natl. Acad. Sci.* **117**, 3375–3381 (2020).

[M33] Bergström, L. Hamaker constants of inorganic materials. *Adv. colloid interface science* **70**, 125–169 (1997).

[M34] Médout-Marère, V. A simple experimental way of measuring the hamaker constant a11 of divided solids by immersion calorimetry in apolar liquids. *J. colloid interface science* **228**, 434–437 (2000).

[M35] Neufeld, P. D., Janzen, A. & Aziz, R. Empirical equations to calculate 16 of the transport collision integrals ω (l, s)* for the lennard-jones (12–6) potential. *The J. Chem. Phys.* **57**, 1100–1102 (1972).

[M36] Virtanen, P. *et al.* Scipy 1.0: fundamental algorithms for scientific computing in python. *Nat. methods* **17**, 261–272 (2020).

[M37] Andreotti, B., Claudin, P. & Pouliquen, O. Measurements of the aeolian sand transport saturation length. *Geomorphology* **123**, 343–348 (2010).

[M38] Andreotti, B. *et al.* Aeolian sand transport and ripple dynamics at and below martian pressure. *TBD* **X**, X (2020).

[M39] Cornelis, W. M., Gabriels, D. & Hartmann, R. A parameterisation for the threshold shear velocity to initiate deflation of dry and wet sediment. *Geomorphology* **59**, 43–51 (2004).

[M40] Iversen, J. D. & Rasmussen, K. R. The effect of wind speed and bed slope on sand transport. *Sedimentology* **46**, 723–731 (1999).

[M41] Jones, J. & Willetts, B. Errors in measuring uniform aeolian sand flow by means of an adjustable trap. *Sedimentology* **26**, 463–468 (1979).

[M42] Li, B., Ellis, J. T. & Sherman, D. J. Estimating the impact threshold for wind-blown sand. *J. Coast. Res.* **70**, 627–632 (2014).

[M43] Zingg, A. Wind tunnel studies of the movement of sedimentary material. In *Proceedings of the 5th Hydraulic Conference Bulletin*, vol. 34, 111–135 (Inst. of Hydraulics Iowa City, 1953).

[M44] Anderson, R. S. & Haff, P. Wind modification and bed response during saltation of sand in air. In *Aeolian Grain Transport 1*, 21–51 (Springer, 1991).

[M45] Charru, F., Mouilleron, H. & Eiff, O. Erosion and deposition of particles on a bed sheared by a viscous flow. *J. Fluid Mech.* **519**, 55–80 (2004).

[M46] Ferdowsi, B., Ortiz, C. P., Houssais, M. & Jerolmack, D. J. River-bed armouring as a granular segregation phenomenon. *Nat. communications* **8**, 1–10 (2017).

[M47] Nishimura, K. & Hunt, J. Saltation and incipient suspension above a flat particle bed below a turbulent boundary layer. *J. Fluid Mech.* **417**, 77–102 (2000).

[M48] Rice, M. A., Willetts, B. B. & McEwan, I. An experimental study of multiple grain-size ejecta produced by collisions of saltating grains with a flat bed. *Sedimentology* **42**, 695–706 (1995).

[M49] Rioual, F., Valance, A. & Bideau, D. Experimental study of the collision process of a grain on a two-dimensional granular bed. *Phys. Rev. E* **62**, 2450 (2000).

[M50] Creyssels, M. *et al.* Saltating particles in a turbulent boundary layer: experiment and theory. *J. Fluid Mech.* **625**, 47–74 (2009).

[M51] Werner, B. T. *A physical model of wind-blown sand transport*. Ph.D. thesis, California Institute of Technology (1987).

[M52] Werner, B. & Haff, P. The impact process in aeolian saltation: two-dimensional simulations. *Sedimentology* **35**, 189–196 (1988).

[M53] Schmeeckle, M. W., Nelson, J. M., Pitlick, J. & Bennett, J. P. Interparticle collision of natural sediment grains in water. *Water Resour. Res.* **37**, 2377–2391 (2001).

[M54] Evans, B. & Goetze, C. The temperature variation of hardness of olivine and its implication for polycrystalline yield stress. *J. Geophys. Res. Solid Earth* **84**, 5505–5524 (1979).

[M55] Courtney, T. H. *Mechanical behavior of materials* (Waveland Press, 2005).

[M56] Domokos, G., Jerolmack, D. J., Kun, F. & Török, J. Plato's cube and the natural geometry of fragmentation. *arXiv preprint arXiv:1912.04628* (2019).

[M57] Millour, E. *et al.* The mars climate database (mcd version 5.3). In *Geophysical Research Abstracts*, vol. 21 (2019).

[M58] Lindal, G. F. *et al.* The atmosphere of titan: An analysis of the voyager 1 radio occultation measurements. *Icarus* **53**, 348–363 (1983).

[M59] Bourke, M. C. *et al.* Extraterrestrial dunes: An introduction to the special issue on planetary dune systems. *Geomorphology* **121**, 1–14 (2010).

[M60] Gladstone, G. R. *et al.* The atmosphere of pluto as observed by new horizons. *Science* **351**, aad8866 (2016).

[M61] Tyler, G. *et al.* Voyager radio science observations of neptune and triton. *Science* **246**, 1466–1473 (1989).

[M62] Flasar, F. *et al.* Titan's atmospheric temperatures, winds, and composition. *Science* **308**, 975–978 (2005).

[M63] Basilevsky, A. T. & Head, J. W. The surface of venus. *Reports on Prog. Phys.* **66**, 1699 (2003).

[M64] Mahaffy, P. R. *et al.* Abundance and isotopic composition of gases in the martian atmosphere from the curiosity rover. *Science* **341**, 263–266 (2013).

[M65] Niemann, H. *et al.* The abundances of constituents of titan's atmosphere from the gcms instrument on the huygens probe. *Nature* **438**, 779–784 (2005).

[M66] Fegley Jr, B. & Treiman, A. H. Chemistry of atmosphere-surface interaction on venus and mars. *Venus Mars: atmospheres, ionospheres, solar wind interactions* **66**, 7–71 (1992).

[M67] Kok, J. F., Parteli, E. J., Michaels, T. I. & Karam, D. B. The physics of wind-blown sand and dust. *Reports on progress Phys.* **75**, 106901 (2012).

[M68] Barnes, J. W. *et al.* Spectroscopy, morphometry, and photoclinometry of titan's dunefields from cassini/vims. *Icarus* **195**, 400–414 (2008).

[M69] Smith, B. A. *et al.* Voyager 2 at neptune: Imaging science results. *Science* **246**, 1422–1449 (1989).

[M70] Bourova, E. & Richet, P. Quartz and cristobalite: high-temperature cell parameters and volumes of fusion. *Geophys. research letters* **25**, 2333–2336 (1998).

[M71] Hill, R. E. & Boettcher, A. Water in the earth's mantle: melting curves of basalt-water and basalt-water-carbon dioxide. *Science* **167**, 980–982 (1970).

[M72] Gromnitskaya, E., Stal'gorova, O., Brazhkin, V. & Lyapin, A. Ultrasonic study of the nonequilibrium pressure-temperature diagram of h 2 o ice. *Phys. Rev. B* **64**, 094205 (2001).

[M73] Gregoryanz, E., Clouter, M., Rich, N. & Goulding, R. Raman and brillouin spectroscopic studies of ch 4 single crystals in phases i and ii. *Phys. Rev. B* **58**, 2497 (1998).

[M74] Yamashita, Y., Kato, M. & Arakawa, M. Experimental study on the rheological properties of polycrystalline solid nitrogen and methane: Implications for tectonic processes on triton. *Icarus* **207**, 972–977 (2010).

[M75] Bezuglyi, P. Sound velocity and elastic and thermal characteristics of crystalline nitrogen and oxygen. *Phys. Solid State* **10**, 1660–1664 (1969).

[M76] Jerolmack, D. J. *et al.* Internal boundary layer model for the evolution of desert dune fields. *Nat. Geosci.* **5**, 206–209 (2012).

[M77] Cruikshank, D. P. *et al.* A spectroscopic study of the surfaces of saturn's large satellites: H2o ice, tholins, and minor constituents. *Icarus* **175**, 268–283 (2005).

[M78] Hörst, S. & Tolbert, M. A. In situ measurements of the size and density of titan aerosol analogs. *The Astrophys. J. Lett.* **770**, L10 (2013).

[M79] Satorre, M. *et al.* Density of ch4, n2 and co2 ices at different temperatures of deposition. *Planet. Space Sci.* **56**, 1748–1752 (2008).

Extended Data

| Domain	Variable		Units	Earth	Mars	Titan	Venus	Pluto	Triton
System	Gravity	g	m/s²	9.81	3.73	1.36	8.88	0.62	0.78
	Pressure	p	kPa	102; 6.7	0.625; 0.25[17,M57]	150; 0.23[M58]	7750; 6500[M59]	0.0105; 0.0001[M60]	0.0017; 0.0004[M61]
	Temperature	T	K	295; 50	204; 122[17,M57]	92; 4[M58,M62]	703; 105[M63]	46; 18[M60]	48; 10[M61]
	Composition			Air	CO_2[M64]	N_2[M65]	CO_2[M66]	N_2[M60]	N_2[M61]
Fluid	Molecular mass	M	g/mol	29	43	27	43	28	28
	Adiabatic index	χ_c	ND	1.4	1.3	1.5	1.2	1.5	1.5
	Density*	ρ_f	kg/m³	1.2; 0.28	0.018; 0.018	5.4; 0.24	58; 57	0.000078; 0.000039	0.00012; 0.000054
	Kinematic viscosity*	v	mm²/s	15.3; 5.55	737; 1100	1.13; 0.101	0.632; 0.693	41800; 35000	27600; 17800
	Mean free path*	λ	μm	0.0655; 0.0183	4.43; 5.60	0.00845; 0.000573	0.00215; 0.00220	439; 290	288; 156
	Speed of sound*	c	m/s	344; 29.2	224; 68.5	202; 4.40	407; 30.5	141; 27.9	145; 15.1
Solid	Composition			Quartz; Gypsum	Basalt[M67]; Quartz[M67]	Tholin[4,M68]; Water[4]	Basalt[M66]; Quartz[M66]	Tholin[M69]; Methane[3]; Nitrogen[3]	Methane[32]; Nitrogen[32]
	Elastic modulus*	E	GPa	108; 1.73[4,M70] / 37.8; 3.48[4]	96.1; 4.76[4,M71] / 111; 4.23[4,M70]	15.8; 0.104[4] / 9.68; 0.0853[M72]	76.6; 4.10[4,M71] / 93.5; 3.64[4]	16.9; 0.260[4] / 27.9; 3.71[M73] / 1.57; 0.346[M74,M75]	27.5; 2.06[M73] / 1.54; 0.192[M74,M75]
	Yield stress*	Y	GPa	31.9; 0.37 / 13.6; 1.10	29.4; 1.10 / 32.6; 0.877	6.17; 0.038 / 3.91; 0.0324	24.7; 1.05 / 28.8; 0.846	6.59; 0.0931 / 10.4; 1.24 / 0.686; 0.146	10.2; 0.690 / 0.670; 0.0814
	Poisson ratio	V	ND	0.2[4] / 0.3[4]	0.2[4] / 0.2[4]	0.35[4] / 0.31[M72]	0.2[4] / 0.2[4]	0.35[4] / 0.26[M73] / 0.3[M75]	0.26[M73] / 0.3[M75]
	Density	ρ_s	kg/m³	2650[9] / 2380[M76]	3000[M67] / 2650[9]	1400[M77,M78] / 950[M72]	3000[M67] / 2650[9]	1400[M77,M78] / 470[M79] / 940[M79]	470[M79] / 940[M79]
	Surface energy*	γ	mJ/m²	59.7; 0.274 / 74.9; 0.110	85.8; 0.420 / 59.3; 0.622	76.7 / 22.4; 0.462	79.0; 7.39 / 54.4; 6.54	76.7 / 32.7; 0.53 / 21.4; 4.55	32.6; 0.292 / 21.8; 2.55

Table ED1. Variables indicated with an asterisk are derived quantities. 'ND' denotes dimensionless quantities. Cells with one value denote variables assumed to be constant. For cells with two values separated by a semi-colon, the first is the average of the value at T and/or p extremes and the second is the range. References are given for non-derived quantities (aside from well-known values) and measurements needed for temperature-dependent elastic modulus (Methods M7). Only the predominant mineral or molecule is written in the composition rows of this table for brevity. Tholin in this table is referred to as 'Tholin (Dense)' in the figure legends; 'Tholin (Light)' has a lower yield stress (Methods M7) and a lower density of 400 kg/m³.
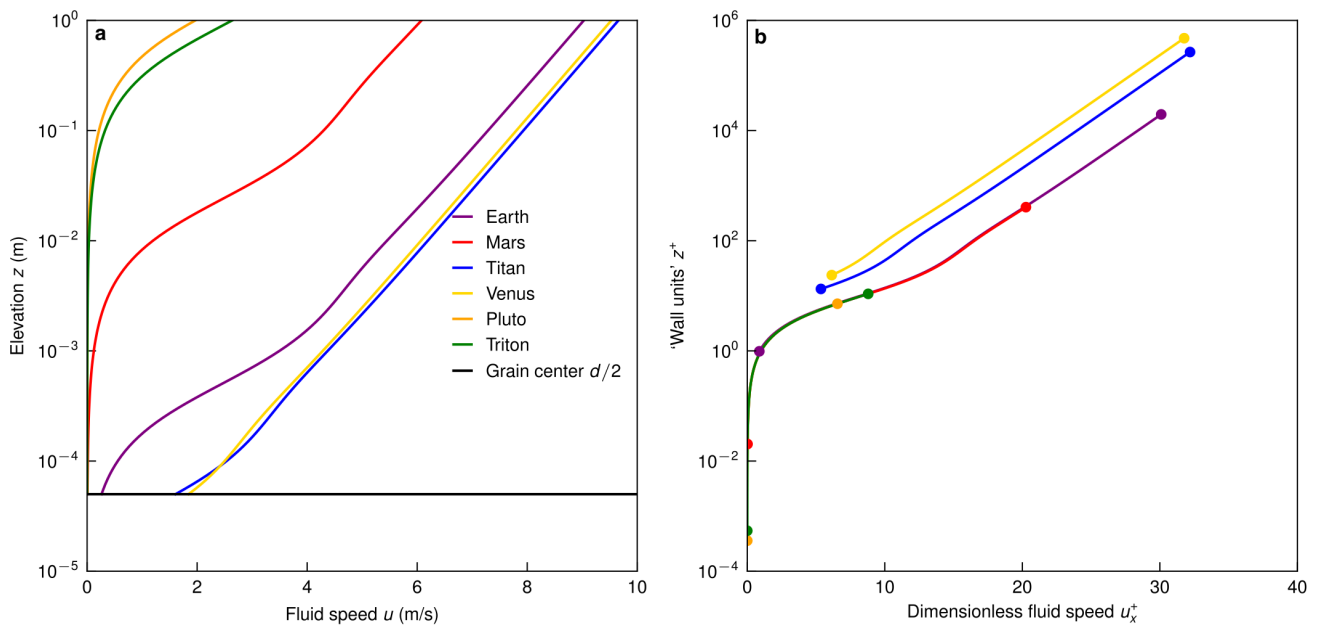
Figure ED1. Wind profiles. (a) Mean horizontal wind speed with elevation for a fixed friction velocity ($u_* = 0.3$ m/s) and grain size ($d = 100$ μm) for the six bodies of interest using the empirical relation in Text S4. The grain center is denoted with a black line. **(b)** Dimensionless presentation of **(a)**, where $u_x^+ = u/u_*$ and $z^+ = zu_*/\nu$.
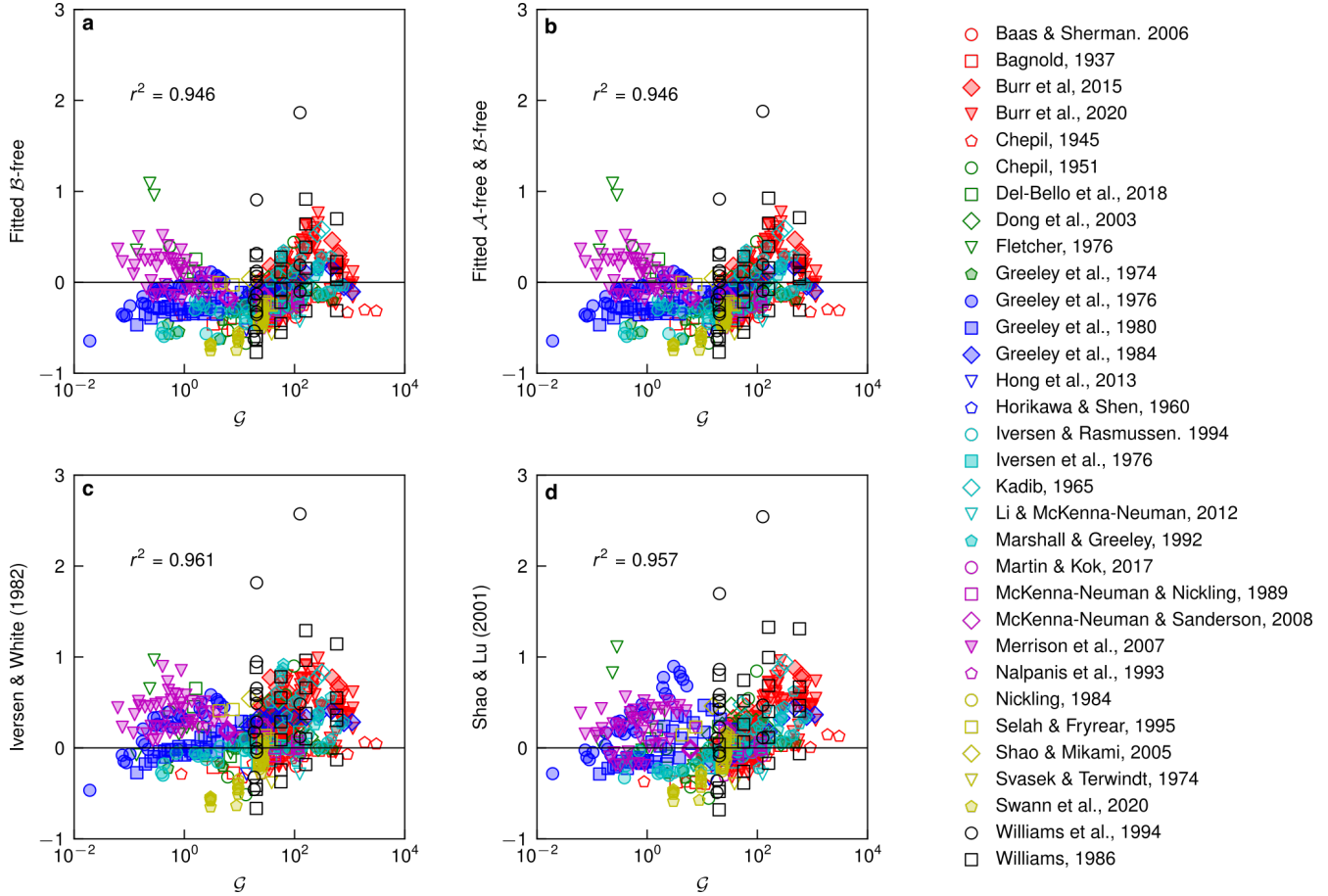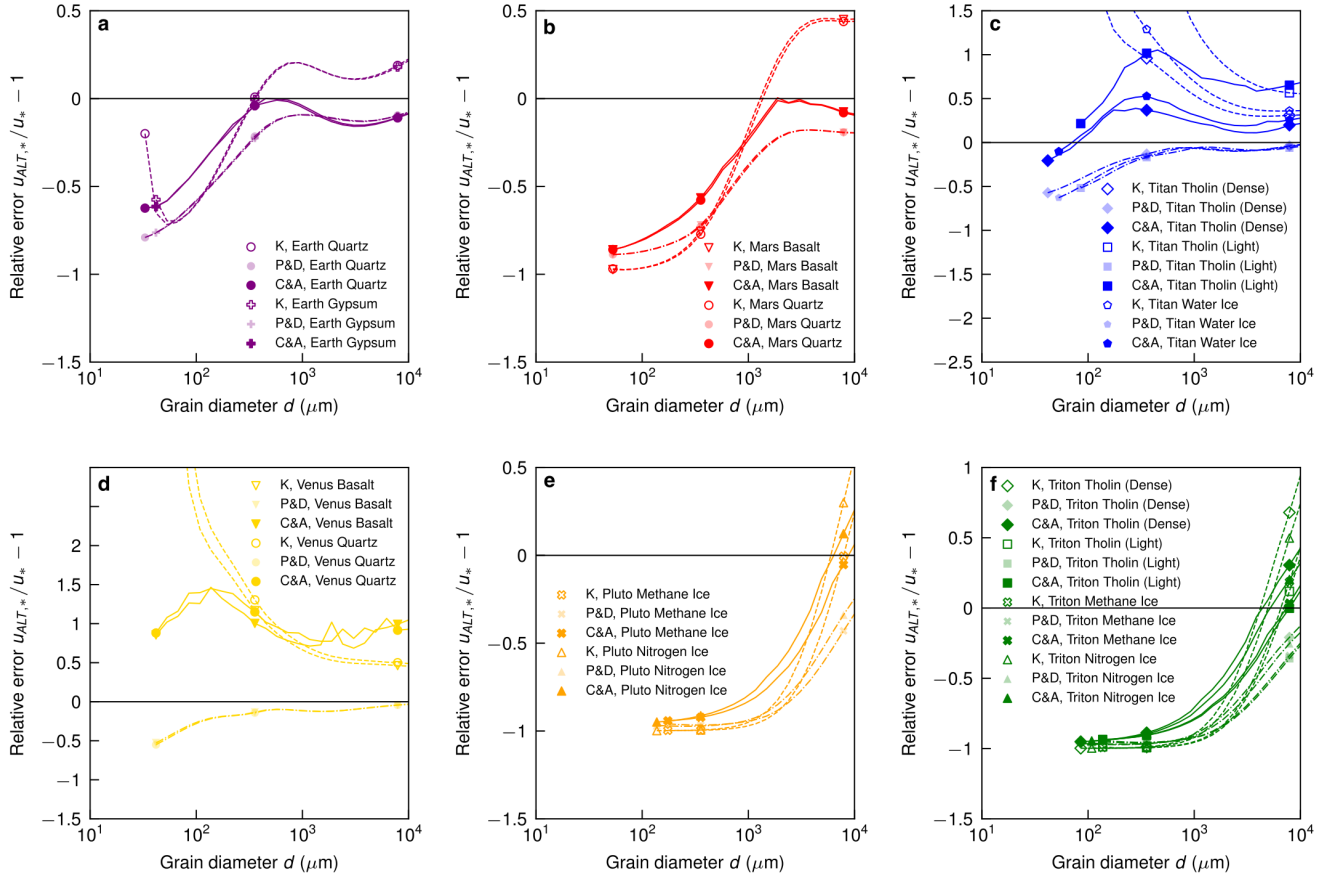
Figure ED2. Fluid threshold prediction comparison to data. Four methods for predicting the fluid threshold are compared to observed data, where the vertical axis is $u_{*,observed}/u_{*,predicted} - 1$ (for the labelled prediction) and the horizontal axis is the Galileo number, $\mathcal{G}$. References for the observations are given on the right, where markers with shaded interiors signify experiments not using standard Earth conditions. The correlation coefficient (r^2) for each log-log comparison of $u_{*,observed}$ versus $u_{*,predicted}$ (i.e. Figure 2c) is annotated. **(a)** The prediction in the main text, where $\mathcal{A} = 1$. **(b)** The prediction except $\mathcal{A}$ is a free-parameter. **(c)** The prediction using the empirical relation of Iversen & White (1982)[9]. **(d)** The prediction using the semi-empirical theory of Shao & Lu (2000)[8].
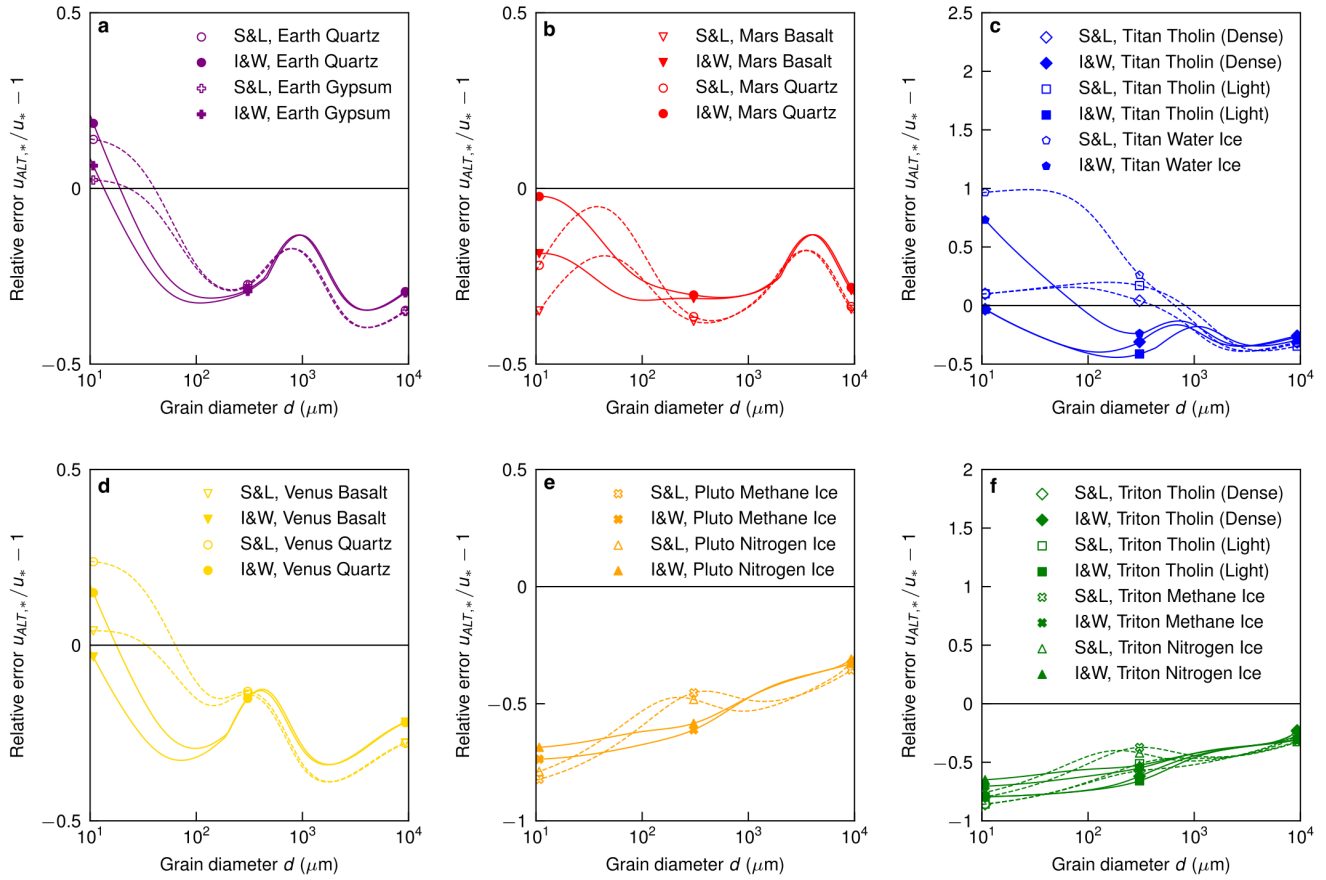
Figure ED3. Fluid threshold prediction comparison to each other. The relative error between the alternative predictions of Shao & Lu (2000)[8] (S&L) and Iversen & White (1982)[9] (I&W) with the prediction in the main text for the fluid threshold for average conditions on each body. Each sediment candidate is given for **(a)** Earth, **(b)** Mars, **(c)** Titan, **(d)** Venus, **(e)** Pluto and **(f)** Triton.
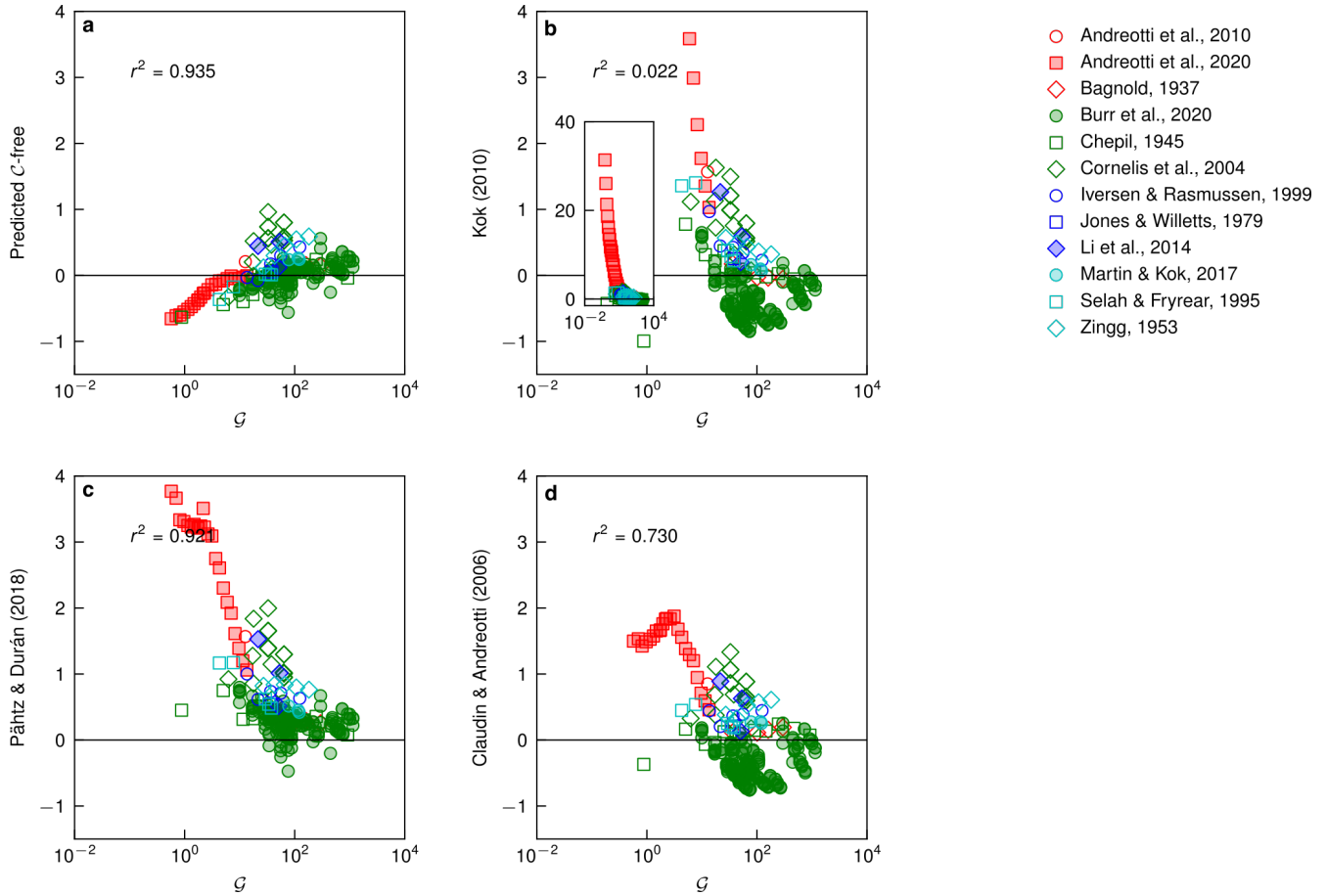
Figure ED4. Impact threshold prediction comparison to data. Four methods for predicting the impact threshold are compared to observed data, where the vertical axis is $u_{*,observed}/u_{*,predicted} - 1$ (for the labelled prediction) and the horizontal axis is the Galileo number, $\mathcal{G}$. References for the observations are given on the right, where markers with shaded interiors signify experiments not using standard Earth conditions or field data. The correlation coefficient (r^2) for each log-log comparison of $u_{*,observed}$ versus $u_{*,predicted}$ (i.e. Figure 3c) is annotated. **(a)** The prediction in the main text. **(b)** The prediction using the semi-empirical theory of Kok (2010)[5] (note: the vertical axis bounds are extended in the inset to show the full data extent). **(c)** The prediction using the semi-empirical theory of Pähtz & Durán (2018)[6]. **(d)** The prediction using the semi-empirical theory of Claudin & Andreotti (2006)[7].

Figure ED5. Impact threshold prediction comparison to each other. The relative error between the alternative predictions of Kok (2010)[5] (K), Pähtz & Durán (2018)[6] (P&D) and Claudin & Andreotti (2006)[7] (C&A) with the prediction in the main text for the impact threshold for average conditions on each body. Each sediment candidate is given for **(a)** Earth, **(b)** Mars, **(c)** Titan, **(d)** Venus, **(e)** Pluto and **(f)** Triton.
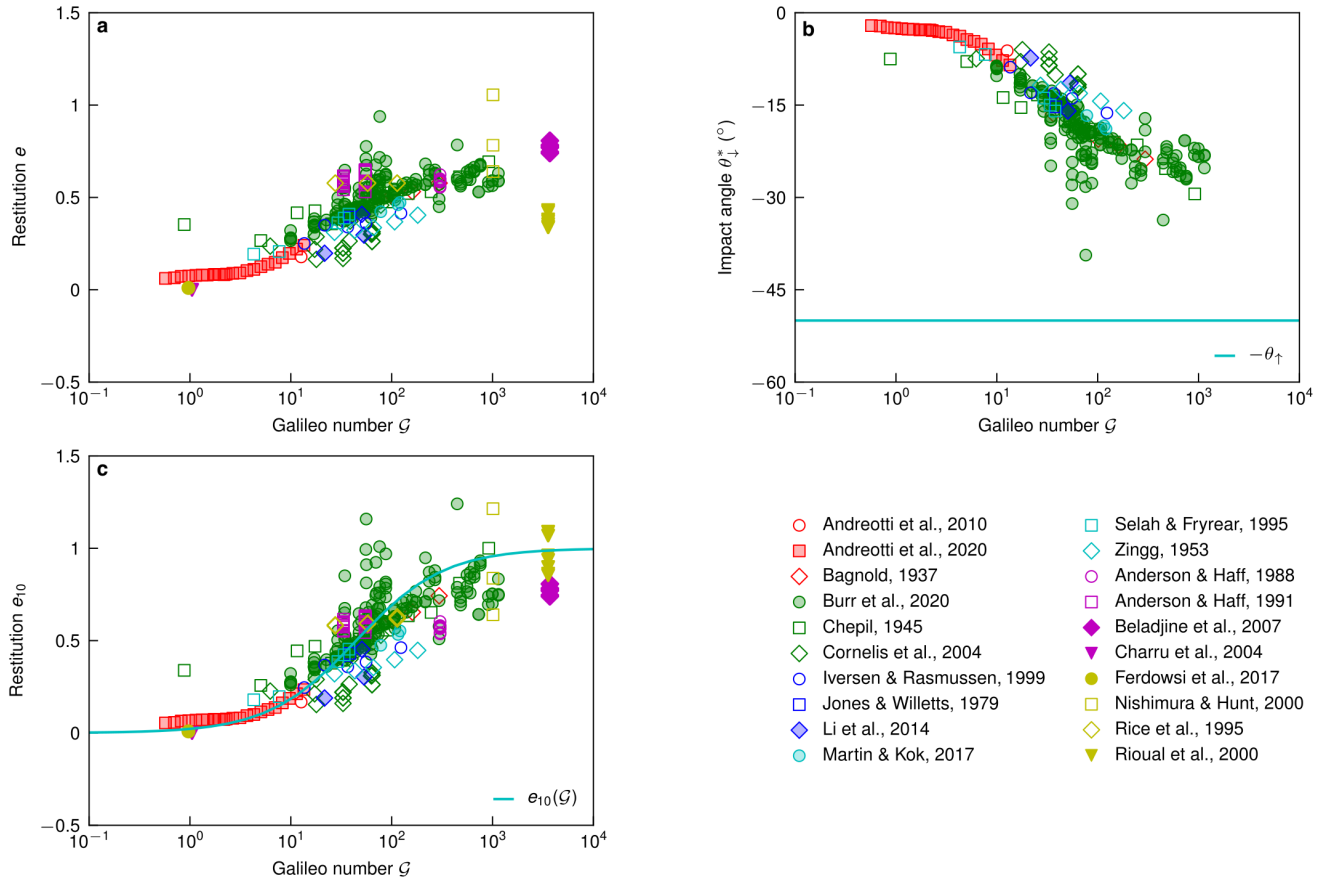
Figure ED6. Restitution mechanics and empirical fit. References for the observations are given on the bottom right, where markers with shaded interiors signify experiments not using standard Earth conditions or field data, markers with solid interiors signify explicit measurements of the restitution coefficients outside wind tunnels. Magenta and yellow markers are from studies where the restitution coefficient is measured or noted, values for the vertical-axes of markers with other colors are inferred from simulated trajectories. All horizontal-axes are the Galileo number $\mathcal{G}$. **(a)** The ratio of the ejection to impact velocity of a characteristic saltating grain, i.e. the restitution coefficient e. **(b)** The angle the grain impacts the bed, with the theoretical fixed ejection angle denoted (cyan line). **(c)** The restitution coefficient normalized such that it impacted the bed at a fixed angle ($\theta_\downarrow = -10\,^\circ$), e_{10}, with the empirical relationship used in the main text relating the two axes (cyan line) (Methods M6).
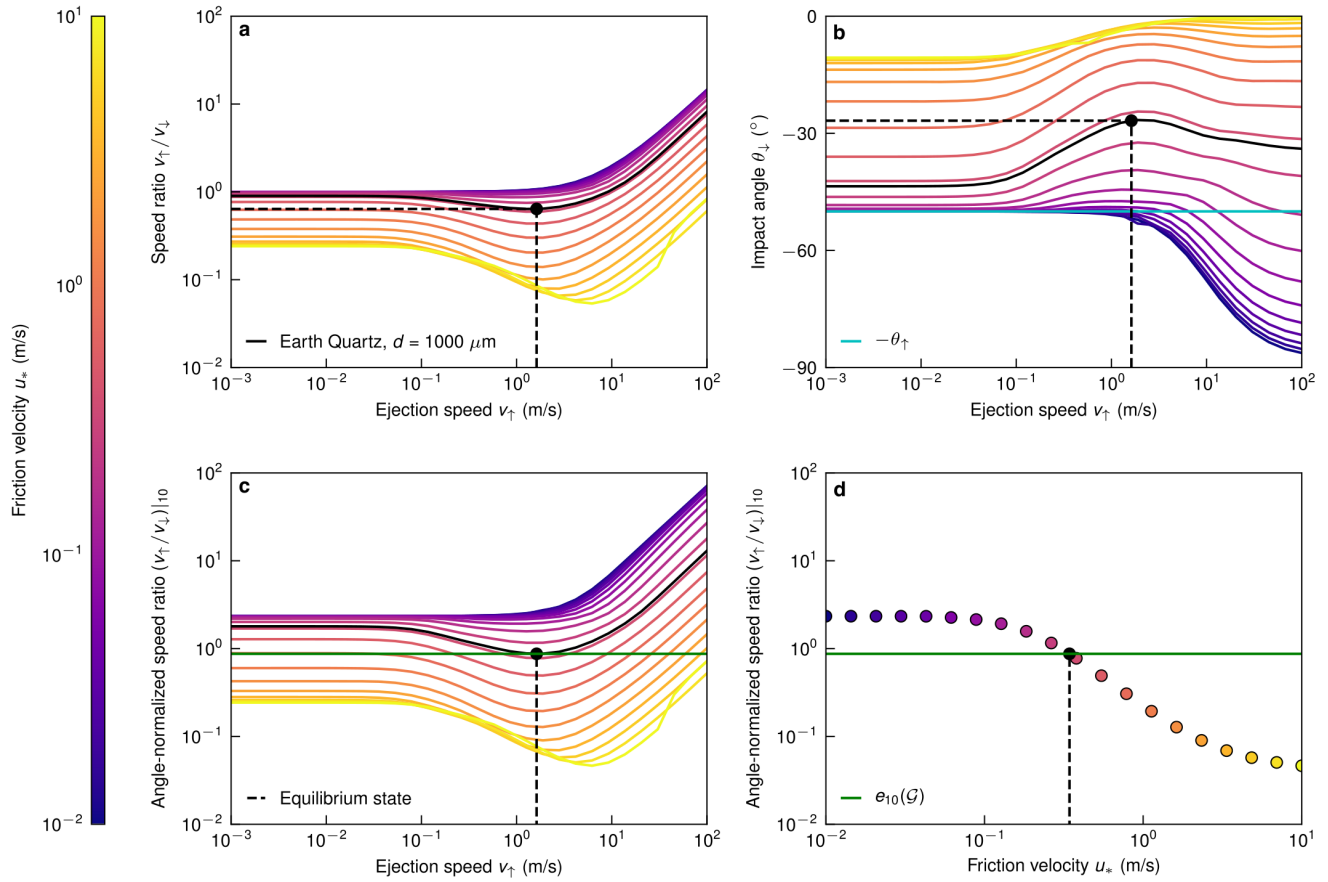
Figure ED7. Trajectory analysis example. (a-c) Each point on the lines with color corresponding to the colorbar on the left are for a trajectory of a 1 mm Quartz grain at average Earth conditions leaving the bed with a ejection velocity of $v_\uparrow$ from the horizontal axis. The solid black line denotes the impact threshold friction velocity, while the black dot and the corresponding dashed black lines denote the unique pair of the friction velocity and ejection velocity at the impact threshold. **(a)** The ratio of the ejection to impact speeds for a trajectory. **(b)** The impact angle for a trajectory, with the cyan line indicating the ejection angle. **(c)** The ratio of the ejection to impact speeds for a trajectory, normalized as if the impact angle was fixed ($\theta_\downarrow = -10\,^\circ$), e_{10} (Methods M6). The green line (also in **(d)**) is the 'target' restitution coefficient for this case using the empirical relation found in Figure ED6c. **(d)** The minima for each line in **(c)** plotted against the friction velocity. We define the impact threshold as the intersection of the trend and the green line.
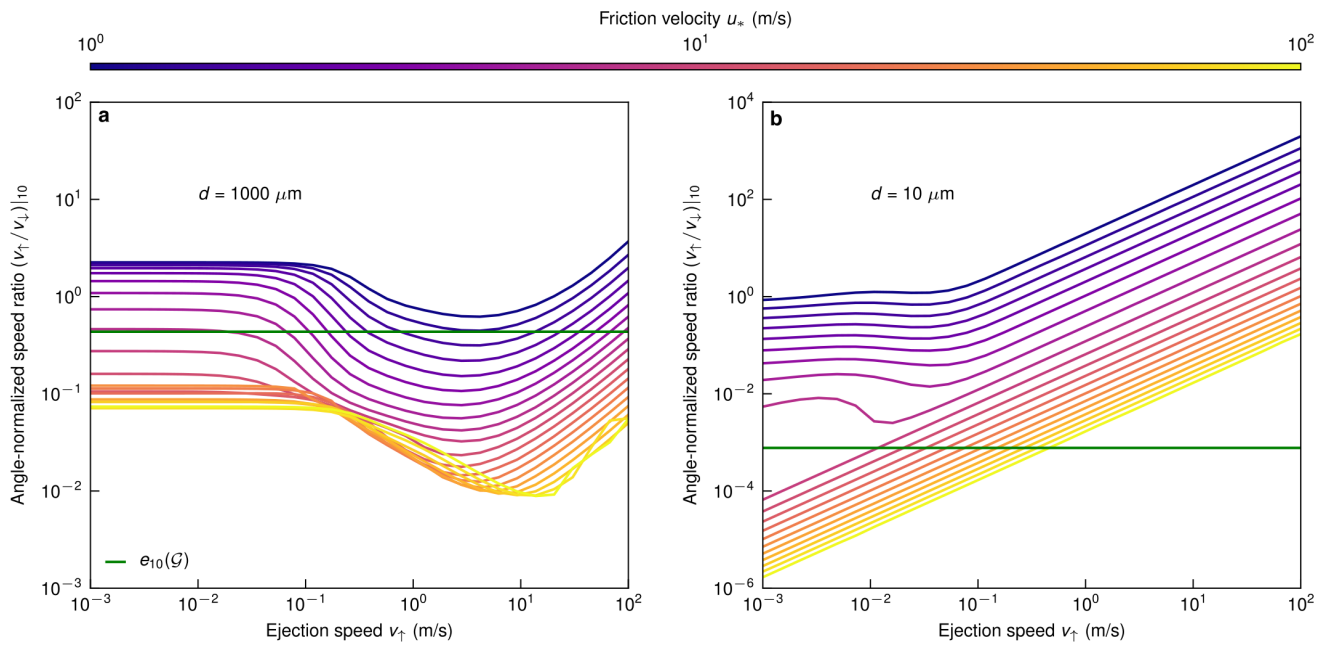
Figure ED8. Contrasting trajectory examples. Trajectories like Figure ED7c for Basalt grains at average Mars conditions of size (**a**) $d = 1$ mm and (**b**) $d = 10\ \mu$m. The green lines are the 'target' restitution coefficient for each case using the empirical relation found in Figure ED6c. The qualitatively different behavior in the neighborhood of the solution shows how this formulation of the impact threshold loses meaning for small grains. The minima for each successive curve of fixed friction velocity in (**a**) are close and transition smoothly, and u_* and $v_\uparrow$ are not extremely different. This is in contrast with (**b**), where the minima close to the target restitution rapidly diverges as u_* changes, and $v_\uparrow$ is extremely small at the minima relative to u_*.
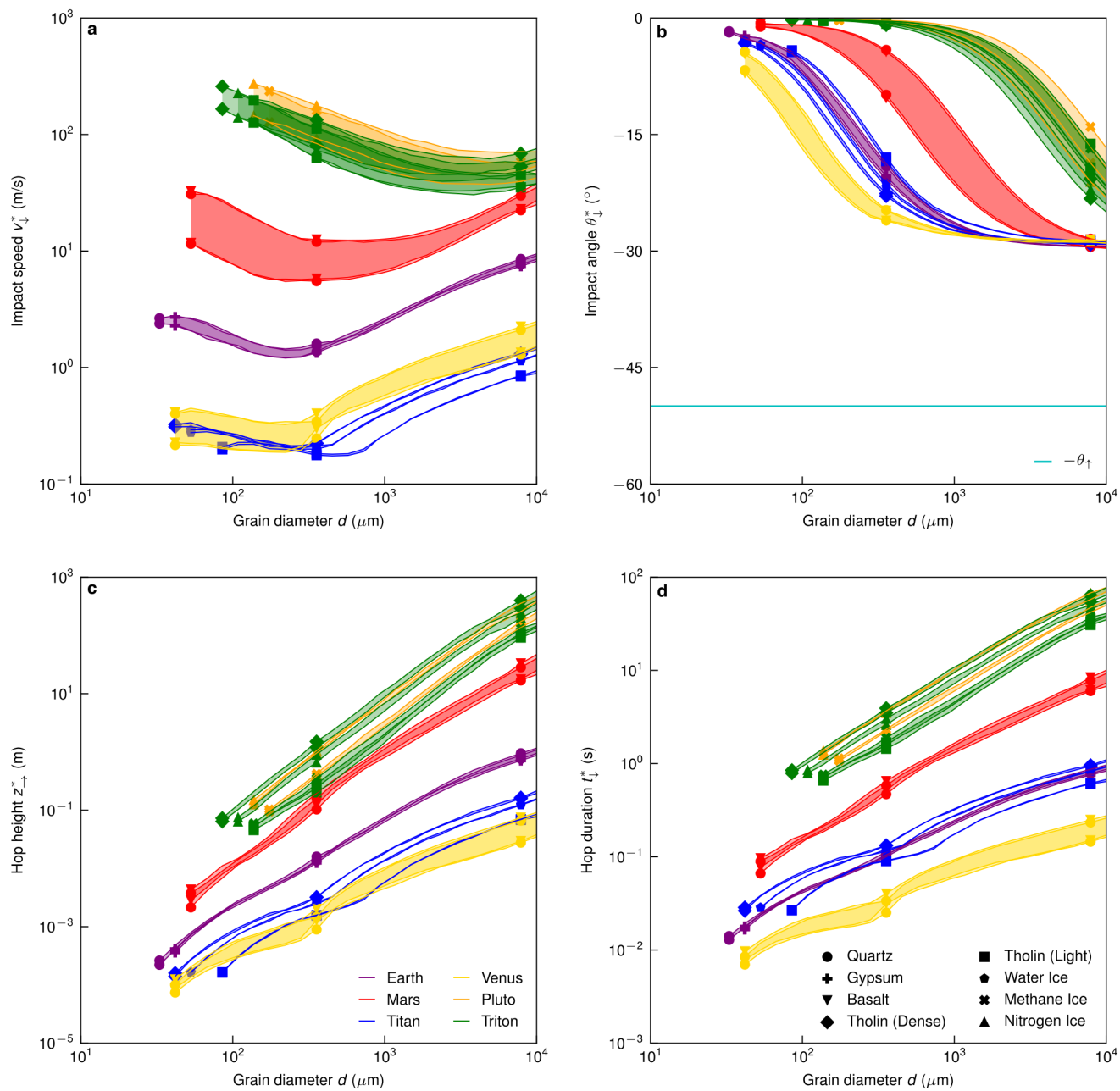
Figure ED9. Trajectory diagnostics. Predictions for the characteristic saltator trajectory at the impact threshold with varying grain diameter for **(a)** impact speed, **(b)** impact angle, **(c)** hop height and **(d)** hop duration. Bands show the range for different candidate and known minerals on each planetary body (see legends in **(c)** and **(d)**) based on known temperature and pressure variability.

Supplementary Information

Body	Image Code	Hyperlink
Earth	PIA11084	https://photojournal.jpl.nasa.gov/catalog/PIA11084
Mars	V77742003	http://viewer.mars.asu.edu/planetview/inst/themis/V77742003
Titan	PIA14500	https://photojournal.jpl.nasa.gov/catalog/PIA14500
Venus	N/A	https://lpi.usra.edu/publications/slidesets/venus/slide_18.html
Pluto	PIA20213	https://photojournal.jpl.nasa.gov/catalog/PIA20213
Triton	PIA02214	https://photojournal.jpl.nasa.gov/catalog/PIA02214

Table S1. Information on the dune imagery in Figure 1.

Calculation	Variable	Units	Material	Value
Viscosity	σ	Å	Air	3.617[12]
			CO_2	3.996[12]
			N_2	3.667[12]
			Ar	3.432[12]
			CH_4	3.780[12]
	ε_T/k_B	K	Air	97[12]
			CO_2	190[12]
			N_2	99.8[12]
			Ar	122.4[12]
			CH_4	154[12]
	M	g/mol	Air	28.964
			CO_2	44.01
			N_2	28.013
			Ar	39.948
			CH_4	16.04
Adhesion	$n_s(\lambda,T)$	ND(μm,K)	CH_4	1.3310(63.28,30)[S1]
			CH_4	1.3310(63.28,90)[S1]
			Quartz	1.4575(63.28,300)[S2]
			Quartz	1.4566(63.28,180)[S2]
			Gypsum	1.5218(57.30,288)[S3]
			Gypsum	1.5190(57.30,378)[S3]
			Basalt	1.5690(59.00,296)[S4]
			H_2O	1.2603(63.28,90)[S5]
			H_2O	1.2464(63.28,70)[S5]
			N_2	1.22(63.28,22)[M79]
			N_2	1.20(63.28,10)[M79]
	$\varepsilon(T)$	ND(K)	CH_4	1.725(80)[S6]
			Quartz	3.8[13]
			Gypsum	5.7[S7]
			Basalt	3.8[13]
			H_2O	250(90)[S8]
			N_2	1.462(47.9)[S9]
	$n_f(\lambda,T,p)$	ND(μm,K,Pa)	Air	1.00027180(63.28,293,101325)[S10]
			Air	1.00022554(63.28,353,101325)[S10]
			CO_2	1.00005440(63.28,288,13170)[S11]
			CO_2	1.00039706(63.28,323,105360)[S11]
			N_2	1.00003581(63.28,288,13170)[S11]
			N_2	1.00026470(63.28,323,105360)[S11]
Yield speed	$E_0(T_0)$	GPa(K)	CH_4	33.12(20.5)[M73]
			Quartz	107.5(300)[4]
			Gypsum	37.44(300)[4]
			Basalt	92.31(300)[4]
			H_2O	10(77)[M72]
			N_2	1.747(37)[M74]
			Tholin	10.38(300)[4]
	T_m	K	CH_4	90.67[M73]
			Quartz	1700[M70]
			Gypsum	419
			Basalt	1333[M71]
			H_2O	273
			N_2	64[M74]
			Tholin	350[4]

Table S2. Measured constants for calculations of the fluid viscosity (Methods M4), particle adhesion (Methods M2) and particle yield speed (Methods M7) used in this study. References are given for each value, aside from the molar mass which is readily available. We could not source data for Basalt refractive index at another temperature than the one above, so we assume no temperature dependence. Static relative permittivity (ε) in solids is sensitive to temperature at low temperature; measurements found at temperatures similar to the planetary body temperatures we are interested in are given. ε was assumed to be 1 for all gases[13].

S1 Alternative fluid threshold predictions

The two fluid threshold prediction theory alternatives we compare our results to are Iversen & White (1982) and Shao & Lu (2000)[8,9]. We chose these over other alternatives because they have been employed extensively in planetary aeolian geomorphology[M67], and provide similar results through contrasting approaches. See Figures ED2 & ED3 for comparisons with the results presented in this paper.

Iversen & White (1982) non-dimensionalize the important parameters in an intuitive way and then use a correlative empirical approach to create an accurate interpolative piece-wise prediction[9],

$$
u_* \sqrt{\frac{\rho_f}{\rho_s g d}} =
\begin{cases}
0.129 \sqrt{\dfrac{1 + \frac{6 \cdot 10^{-7}}{\rho_s g d^{\frac{5}{2}}}}{1.928 \mathcal{R}_\tau^{0.092} - 1}} & , 0.003 < \mathcal{R}_\tau \leq 10 \\[4ex]
0.120 \sqrt{1 + \frac{6 \cdot 10^{-7}}{\rho_s g d^{\frac{5}{2}}}} \left(1 - 0.0858 e^{-0.0671(\mathcal{R}_\tau - 10)}\right) & , 10 < \mathcal{R}_\tau
\end{cases}
,
$$

where $\mathcal{R}_\tau = u_* d / \nu$. This method is very accurate (Fig. ED2c), but is not grounded in physical theory and therefore extrapolation is questionable.

Shao & Lu (2000), on the other hand, maintain accuracy (Fig. ED2d) while using a functional form that is inspired by the torque balance in Methods M1,

$$
u_* = \sqrt{A_{SL} \left(\frac{\rho_s g d}{\rho_f} + \frac{\gamma_{SL}}{\rho_f d}\right)},
$$

where $A_{SL} = 0.0123$ and $\gamma_{SL} = 3 \cdot 10^{-4}$ kg/s^2. This approach is intuitive, and Equation 1 has reminiscent scaling with grain diameter; however, some important details and parameterizations are not considered (for example, the dependence of the drag coefficient on Reynolds number).

S2 Alternative impact threshold predictions

The three impact threshold prediction theory alternatives we compare our result to are Kok (2010), Pähtz & Durán (2018) and Claudin & Andreotti (2006)[5–7]. We chose these over other alternatives because they have been employed extensively, iterated upon, and provide contrasting approaches. See Figures ED4 & ED5 for comparisons with the results presented in this paper. For brevity, since all of these theories require multiple relationships and numerical methods to solve, we do not write the full theories here as we did for the fluid threshold (Methods S1). A short description of each approach pertinent to comparison is given instead.

The approach in Kok (2010) is to couple depth- and particle ensemble-averaged quantities within the saltation layer[5]. This method uses 6 fit parameters. This approach finds that, no matter the environment, the minimum threshold friction velocity is approximately universal. This is mostly because the sub-layer is not resolved, neglecting the effect of viscosity in how friction velocity and near-bed fluid speed are related. Because of this, the predictions are quite insensitive to experimental conditions since the grain sizes used are near the neighborhood of this common minimum (Fig. ED4b).

Pähtz & Durán (2018) couple equations for the characteristic horizontal fluid and particle speeds, the vertical particle speed and the saltation layer height[6]. This method also has 6 fit parameters. In our implementation of their approach we include their implementation of 'cohesion', however when comparing their prediction to measurements we assume all particles have the elastic modulus value of $E = 70$ GPa they reference for quartz in the paper, in lieu of reported values for all sediment materials. We did, however, test that the results were not sensitive to this choice over the range of likely values, and note that their cohesion number C_{PD} only goes weakly with E; $C_{PD} \propto E^{-1/5}$. We employ the same fluid flow profile as this approach[M1] (Text S4), but suspect the largest deviation from our approach — in lower-density environments — is due to the drag coefficient implementation and the loss of grain diameter sensitivity via the scaling of C_{PD}.

Our approach for the threshold builds on Claudin & Andreotti (2006)[7]. In their implementation that has 5 fit parameters, they find the steady-state trajectory (without lift) as in Methods M5 but enforce an ejection velocity:

$$
v_\uparrow = a_{CA} \sqrt{g d \left(1 + \frac{3}{2} \left(\frac{d_{m,CA}}{d}\right)^{5/3}\right)},
$$

instead of choosing the minimum $v_\uparrow$ that results in the required restitution as we do here. In the equation above, there are two of the fit parameters; they adjust the 'trapping velocity' due to gravity so that the theory fits data (a_{CA}), and include the effect

of cohesion ($d_{m,CA}$). This approach alleviates the ill-posedness of the prediction at small grain diameters, and has since been adjusted so that the impact threshold approaches its fluid counterpart in that limit[25,M38]. This approach ends up parameterizing the momentum loss within an equation for the ejection speed, rather than in the restitution coefficient which is treated as a universal constant.

We also note in our approach that the characteristic saltator impact speed at threshold depends linearly on the friction velocity, $v_\downarrow \approx 7u_*$. We do not employ this approximation anywhere, however it may be useful in future work. This linear scaling it similar to other studies[7,S12], but dissimilar to the approach from Kok (2010) where invariance is enforced[5].

S3 Lift force effects

The fluid threshold balance can be written in the form,

$$u_p^2 = \frac{1}{2\sqrt{2}C_D + C_L}\frac{4}{3}\left(\frac{gd(s-1)}{\mathcal{A}} + 3\sqrt{6}\frac{\gamma e^{-\mathcal{B}}}{d\rho_f \mathcal{A}}\right),$$

where u_p is the fluid speed at the particle center, C_D and C_L are the drag and lift coefficients, respectively, g is gravity, d is the grain diameter, $s = \rho_s/\rho_f$ is the ratio of the solid to fluid densities, $\mathcal{A}$ is the ratio of a sphere with the same diameter to the effective frontal area of the grain, γ is the surface energy and $\mathcal{B}$ is the ratio of the characteristic distance between particles in contact and the contact-scale roughness. Inspecting this equation, we see that the left hand side must be positive, and everything inside the right hand side brackets is also positive. The lift coefficient C_L can be negative when downforce is created by shear. We note that a potentially unimportant but previously unnoticed result (as far as we are aware) from this equation is that if $C_L < -2\sqrt{2}C_D$, the solution for u_p is imaginary.

This is not typically an issue since the lift coefficient is small relative to its drag counterpart and positive in the continuum-limit, however implementing the drag correlation below (Text S5) with theory for the lift coefficient at high Knudsen number in the free-molecular limit[S13] does result in an imaginary solution. We do not present results from this analysis here, since the condition that $\lambda\omega \ll u$, where λ is the mean free path and ω is the shear across the grain required for Taylor expansion in this theory does not hold in the free-molecular cases we study in this paper[S13]. Furthermore, lift in the free-molecular limit is formulated using the probability of molecules striking hemispheres of the grain unequally which depends strongly on proximity to a wall, and this theory assumes no walls (or a bed of grains) is close to the grain unlike the fluid threshold case at hand.

If this transition to a complex solution is required, however, then there is a discontinuity in the threshold fluid threshold relationship $u_*(d)$ when $C_L = -2\sqrt{2}C_D$ unless $\partial\left(2\sqrt{2}C_D + C_L\right)/\partial d\big|_{C_L=-2\sqrt{2}C_D} = 0$ (which does not hold in general). Without a clear theory or data on this potentially moot case we do not discuss it in the main text.

S4 Fluid horizontal flow profile

We employ the following relationship for the horizontal fluid flow (u_x) across all environments from Guo & Julien (2007)[M1],

$$\frac{u_x}{u_*} = 7\arctan\left(\frac{z_p}{7}\right) + \frac{7}{3}\arctan^3\left(\frac{z_p}{7}\right) - 0.52\arctan^4\left(\frac{z_p}{7}\right) + \log\left(1 + \left(\frac{9z_p}{e^{16.873\kappa}}\right)^{\frac{1}{\kappa}}\right) - \frac{1}{\kappa}\log\left(1 + 0.3d_p(1 - e^{\frac{-d_p}{26}})\right),$$

where u_* is the friction velocity, $z_p = zu_*/\nu$ and $d_p = du_*/\nu$ are both Reynolds numbers with ν as the kinematic viscosity and $\kappa = 0.4$ is Von Karman's constant. This relationship is fit to rough-walled pipe flows, where the grain diameters of the roughness elements is d_p, refining the seminal contributions of Nikuradse (1950)[S14]. It is a sum of the Law of the Wall region and the viscous sublayer, with the buffer layer between them, and only characterizes the mean horizontal flow. We neglect turbulent fluctuations here, but note their important role in trajectories, especially for small grains. $z = 0$ is defined as the bottom of a grain resting on the bed.

S5 Drag coefficient correlation

The drag coefficient (C_D) is found through correlative methods to fit experimental data by Loth (2008) in the following form[11],

$$C_D = \begin{cases} \dfrac{C_D^a + \mathcal{M}^4 C_D^b}{1 + \mathcal{M}^4} & , \mathcal{R} \le 45 \\[4mm] \dfrac{24}{\mathcal{R}}\left(1 - \dfrac{0.258C_D^c}{1 + 514C_D^d}\right)\left(1 + 0.15\mathcal{R}^{0.687}\right) + \dfrac{0.42C_D^c}{1 + 42500C_D^d\mathcal{R}^{-1.16}} & , \mathcal{R} > 45 \end{cases},$$

$$C_D^a = \frac{24}{\mathcal{R}} \frac{1 + 0.15\mathcal{R}^{0.687}}{1 + \mathcal{K}(2.514 + 0.8e^{-0.55/\mathcal{K}})},$$

$$C_D^b = \frac{C_D^e}{1 + \left(\frac{C_D^e}{1.63} - 1\right)\sqrt{\frac{\mathcal{R}}{45}}},$$

$$C_D^c = \begin{cases} \dfrac{5 + 2\tanh\left(3\log(\mathcal{M} + 0.1)\right)}{3} & ,\mathcal{M} \leq 1.45 \\[3mm] 2.044 + 0.2e^{-1.8\log(\mathcal{M}/1.5)^2} & ,\mathcal{M} > 1.45 \end{cases},$$

$$C_D^d = \begin{cases} 1 - 1.525\mathcal{M}^4 & ,\mathcal{M} \leq 0.89 \\[3mm] 10^{-4}\left(2 + 8\tanh(12.77(\mathcal{M} - 2.02))\right) & ,\mathcal{M} > 0.89 \end{cases},$$

$$C_D^e = \frac{1 + 2x^2}{x^3\sqrt{\pi}}e^{-x^2} + \frac{4x^4 + 4x^2 - 1}{2x^4}\mathrm{erf}(x) + \frac{2\sqrt{\pi}}{3x},$$

where $x = \mathcal{M}\sqrt{\gamma_C/2}$, $\mathcal{M} = u/c$ is the Mach number and $\mathcal{R} = ud/\nu$ is the Reynolds number. γ_C is the heat capacity ratio, u is the speed of the flow with respect to the grain, c is the speed of sound, d is the grain diameter and ν is the kinematic viscosity. This cumbersome but analytical form has predictive power, and we stress that the empiricism here is not specific to sediment transport. We employ this correlation over alternatives as it is more accurate in the rarefied regime, for example when grains are small on Mars, or most grain diameters on Pluto and Triton. Please see the code associated with this paper for an array-passable implementation of the equations above.

S6 Lift coefficient correlation

The lift coefficient (C_L) is found through correlative methods to fit experimental data by Loth (2008) in the following form[19],

$$C_L = \begin{cases} J_* \dfrac{12.92}{\pi}\sqrt{\dfrac{\omega_*}{\mathcal{R}}} & ,\mathcal{R} \leq 50 \\[4mm] -\omega_*^{\frac{1}{3}}\left(0.0525 + 0.0575\tanh\left(5\log_{10}\left(\dfrac{\mathcal{R}}{120}\right)\right)\right) & ,\mathcal{R} > 50 \end{cases},$$

$$J_* = 0.3\left(1 + \tanh\left(2.5\log_{10}\left(\sqrt{\frac{\omega_*}{\mathcal{R}}} + 0.191\right)\right)\right)\left(0.667 + \tanh\left(6\left(\sqrt{\frac{\omega_*}{\mathcal{R}}} - 0.32\right)\right)\right),$$

where $\omega_* = \omega d/u$, $\mathcal{R} = du/\nu$, and vorticity in the 2D geometry here can be defined $\omega = (u(z = z_p + d/2) - u(z = z_p - d/2))/d$ (where z_p is the particle center elevation, defined as $d/2$ if resting on grains for the fluid threshold). d is the grain diameter, u is the fluid speed relative to the particle at its center and ν is the kinematic viscosity. This correlation is general and not specific to sediment transport, but we stress that there are improvements to be had in its implementation here. Firstly, this lift coefficient assumes the particles can spin and that they are in the bulk flow; neither of these are true in the fluid threshold case. Secondly, there are no rarefaction effects in this formulation. It is likely that the lift coefficient is sensitive to these effects, however no data or theory is available on this issue in the sediment transport geometry[S13]. Nevertheless, we believe this formulation is the most accurate option available.

Auxiliary supplementary information

Table S3. Fluid threshold measurements. All collated data used in the fluid threshold fit for each measurement (Methods M3). Additionally, the phrase used to explain the threshold in the literature is given, as is the wind tunnel name and height. Note that some of the values in this spreadsheet are assumed and not explicitly stated in the paper the threshold measurements are reported, see Methods M3 & M4 for an explanation of how these are calculated. This table is provided as an auxiliary file with the manuscript named 'SI_table3.csv'.

Table S4. Impact threshold measurements. All collated data used in the impact threshold fit for each measurement (Methods M6 & M5). Additionally, the phrase used to explain the threshold in the literature is given, as is the wind tunnel name and height. Note that some of the values in this spreadsheet are assumed and not explicitly stated in the paper the threshold measurements are reported, see Methods M6 & M4 for an explanation of how these are calculated. This table is provided as an auxiliary file with the manuscript named 'SI_table4.csv'.

Table S5. Restitution coefficient measurements. All collated data used in the impact threshold fit for each measurement (Methods M6). If a cell entry is '-9999' it denotes a parameter that does exist for that experiment (wind tunnel name and height, for example). Note that some of the values in this spreadsheet are assumed and not explicitly stated in the paper the measurements are reported, see Methods M6 & M4 for an explanation of how these are calculated. This table is provided as an auxiliary file with the manuscript named 'SI_table5.csv'.

References

[S1] Martonchik, J. V. & Orton, G. S. Optical constants of liquid and solid methane. *Appl. optics* **33**, 8306–8317 (1994).

[S2] Leviton, D. B. & Frey, B. J. Temperature-dependent absolute refractive index measurements of synthetic fused silica. In *Optomechanical Technologies for Astronomy*, vol. 6273, 62732K (International Society for Optics and Photonics, 2006).

[S3] Tutton, A. E. H. The optical constants of gypsum at different temperatures, and the mitscherlich experiment. *Proc. Royal Soc. London. Ser. A, Containing Pap. a Math. Phys. Character* **81**, 40–57 (1908).

[S4] Kuryaeva, R. & Kirkinskii, V. Influence of high pressure on the refractive index and density of tholeiite basalt glass. *Phys. chemistry minerals* **25**, 48–54 (1997).

[S5] Kofman, V., He, J., ten Kate, I. L. & Linnartz, H. The refractive index of amorphous and crystalline water ice in the uv–vis. *The Astrophys. J.* **875**, 131 (2019).

[S6] Amey, R. L. & Cole, R. H. Dielectric constants of liquefied noble gases and methane. *The J. Chem. Phys.* **40**, 146–148 (1964).

[S7] Lide, D. R. *CRC handbook of chemistry and physics*, vol. 85 (CRC press, 2004).

[S8] Young, K. & Frederikse, H. Compilation of the static dielectric constant of inorganic solids. *J. Phys. Chem. Ref. Data* **2**, 313–410 (1973).

[S9] Ebert, L. & Keesom, W. Preliminary measurements of the dielectric constants of liquid and solid nitrogen. In *Proc. K. Akad. Wet. Amsterdam*, vol. 29, 1188 (1926).

[S10] Ciddor, P. E. Refractive index of air: new equations for the visible and near infrared. *Appl. optics* **35**, 1566–1573 (1996).

[S11] Clergent, Y., Durou, C. & Laurens, M. Refractive index variations for argon, nitrogen, and carbon dioxide at $\lambda = 632.8$ nm (he- ne laser light) in the range 288.15 k t 323.15 k, 0< p< 110 kpa. *J. Chem. & Eng. Data* **44**, 197–199 (1999).

[S12] Almeida, M. P., Parteli, E. J., Andrade, J. S. & Herrmann, H. J. Giant saltation on mars. *Proc. Natl. Acad. Sci.* **105**, 6222–6226 (2008).

[S13] Luo, S., Wang, J., Xia, G. & Li, Z. Lift force on nanoparticles in shear flows of dilute gases: negative or positive? *J. Fluid Mech.* **795**, 443–454 (2016).

[S14] Nikuradse, J. *et al.* Laws of flow in rough pipes. (1950).